Patient-specific Cardiovascular Modeling System using Immersed Boundary Technique

Wee-Beng Tay[a], Yu-Heng Tseng [a,*], Liang-Yu Lin[b] and Wen-Yih Tseng[c]

[a]*High Performance Computing & Environmental Fluid Dynamic Laboratory, Department of Atmospheric Sciences, National Taiwan University, Taipei, Taiwan (yhtseng@as.ntu.edu.tw)*
[b]*National Taiwan University Hospital, Taipei, Taiwan*
[c]*Center for Optoelectronic Biomedicine, National Taiwan University College of Medicine, Taipei, Taiwan*

Abstract. A three-dimensional (3-D), computational fluid dynamics (CFD) based, patient-specific cardiovascular modeling system is under-developed. The system aims to identify possible diseased conditions and facilitate physicians' diagnosis at early stage through the hybrid CFD simulation and time-resolved magnetic resonance imaging (4D-MRI). The CFD simulation is based on the 3-D heart model code developed by McQueen and Peskin, which can simultaneously compute fluid motions and elastic boundary motions using the immersed boundary method. The flow features in the ventricles and their responses are investigated under four different inflow reservoir pressure boundary conditions (RPBC). The simulation accuracy is verified with clinical data in terms of hemodynamics, vorticity, kinetic energy and pressure in the left ventricle of the heart. Results indicate that the variation of flow rates and kinetic energy have been well captured during the diastole and systole phase. Qualitative agreement with experimental data is shown in the vorticity field as well as the vortex formation time, which is an index that indicates the cardiac health of the patient. Large pressure on the left ventricle surface has been observed due to the twisting and stretching of heart during the systole phase as well. The encouraging results indicate the feasibility of capturing the important characteristics of the heart during different phases. However, some discrepancies are found in the pulmonary vein and aorta flow rate between the numerical and experimental data. Further studies are required to investigate and solve the remaining problems before it can be used in the clinical diagnostics.

Keywords: Blood flow, Cardiovascular disease, Magnetic resonance imaging, Left ventricle, Numerical simulation, Vortices
PACS: 47.63.-b, 47.32.C-, 47.11.Bc, 87.19.U-

INTRODUCTION

A three dimensional (3-D), computational fluid dynamics (CFD) based, patient-specific cardiovascular modeling system is under-developed. A successful cardiovascular modeling system should identify possible diseased conditions and facilitate physicians' diagnosis at early stage, which can be achieved through the hybrid CFD simulation and time-resolved magnetic resonance imaging (MRI) before heart failure.

Early research [1] has pointed out that the flow dynamics found in the left ventricle (LV) can reveal important information about the overall cardiac health. This is useful in the early diagnostic of patients with potential heart problems. In fact, the emphasis on the LV of the heart dates back to the 1970s. Early experimental studies found that there is eddy generation in the LV during ventricular filling. It was then thought that this is the main reason for the early partial closure that prevents regurgitation [2]. However, later studies [3-4] show that the valve closure is due to the developing adverse pressure gradient and the flow decelerates well before the flow reverses. Computational studies to investigate natural or prosthetic mitral valve are conducted by Mcqueen and Peskin [5] as early as 1982. Mcqueen and Peskin [6] later successfully developed a 3-D heart simulation based on idealized hemodynamic conditions. In order to accommodate the complex geometries, moving wall and fluid-tissue interaction, the immersed boundary method (IBM) is used. Detailed investigation can be conducted through the simulation of blood flow in the

heart over a cardiac cycle. This approach is much more suitable than other numerical methods using structured or unstructured grids since it allows for large grid deformation and is efficient. With appropriate data on the flow rates and pressures of the heart at different times throughout a cycle, one will be able to visualize and detect any peculiarities which occur within the heart in the simulation. The flow pattern within the ventricles of the heart can also be analyzed in detail.

Vortex formation in LV has also attracted much attention recently. Gharib et al. [7] proposed a new dimensionless number, known as the vortex formation time which can be used as an index to determine the cardiac health of the patient. Due to its dimensionless, the index can be used to compare across different patient groups. It has been shown statistically that healthy volunteers have a vortex formation time between 3.5 and 5.5. However, for patients with remodeling pathologies of the LV such as mitral valve stenosis, the index can be an order higher. On the other hand, for patients with dilated cardiomyopathy, the index drops to around 1.5 to 2.5. This index will be very useful when used concurrently with the CFD simulation results to gauge the cardiac condition of an individual.

It has been showed that the different types of artificial heart valves (mechanical, biological), as well as the ways they open and close, have a significant influence on the flow and vortices generated in the LV[7-8]. This is not surprising since the valves alter the inflow and, hence, affect the flow dynamic thereafter. A non-dimensional formation number (FN), similar to that proposed in Gharib et al. [7], has also been used by Pierrakos and Vlachos [9] to assess the efficiencies of different heart valves types. It was found that the critical FN can be used as a parameter to quantify the LV filling process and the performance of the heart valves. Fortini et al. [10] experimentally investigated the effect of mechanical heart valves (MHV) on the flow characteristic of the blood inside a modeled LV. The three types of tested MHV are (a) a one-way, hydraulic valve; (b) a monoleaflet valve; and (c) a bileaflet valve. The first configuration most resembles the natural valve while the modeled LV is a silicone rubber conical sack, which is flexible and transparent. A comparison of vorticity shows that valve (a) gives the simplest plot with just two oppositely signed vortices while the vorticity fields generated by valves (b) and (c) are more complicated. Four to five vortices are generated and are less orderly compared to the valve (a) case.

Other numerical studies of flow within LV also showed the complexity of vortex formation. Domenichini et al. [8] used a mixed spectral-finite differences method to simulate the 3-D fluid dynamics inside the LV of the heart during diastole. They analyzed the sensitivities of several governing parameters, including the eccentricity, Stokes number and Strouhal number. It was found that there is a well-defined structure of vortices regardless of these parameters. As the eccentricity increases, the flow field changes smoothly from almost axisymmetric to complex 3-D structures when the values are similar to the physiological ones. The effect of Stokes number on the flow is rather weak. On the other hand, as Strouhal number decreases, the effect of convection increases and the entry jet extends more deeply into the ventricle. Instability may follow and result in weak turbulence. However, their simplified model only comprises of the LV of the heart. Hence, a more sophisticated simulation including the entire 3-D heart and detailed inflow/outflow information is required. Nevertheless, their analysis theoretically presented the possible flow structure associated with different parameters.

Pedrizzetti and Domenichini et al.[11] numerically investigated the flow-driven opening of a valvular leaflet. This is achieved by analyzing the dynamics of an accelerated stream in a 2-D channel, where the rigid inertialess movable leaflet is initially closed. A version of the immersed boundary is used to account for the moving leaflet and the fluid structure interaction (FSI). The simulation is carried out by varying the Strouhal number and changing the temporal law ($V(t) = (1-\cos(\pi t))/2$, where $V(t)$ is the dimensionless discharge). Three stages of the flow phases are identified in general. Initially, the valve opens quickly without significant shedding. Later on, the leaflet greatly slows down and a primary vortex is formed from the trailing valvular edge. The vortex then grows and becomes ejected. The last stage corresponds to the presence of a stable vortex-sheet wake and slow leaflet motion. The actual timing depends on the Strouhal number and temporal law. However, their test is limited in 2-D and only served as a starting point for more complicated simulation. Both numerical and experimental studies for different types and configurations of the valves show that the valves must be accurately mimicked in the design of the simulation. Any discrepancy will give erroneous results in the flow and vortex formation in the LV.

Cheng et al. [12] also simulated the LV filling of the heart using a commercial software, ADINA-FSI. The LV is modeled using a 3-D thin-walled ellipsoid, prescribed by a time-varying Young's modulus. The simulation allows the use of non-linear, anisotropic material properties and large deformation. Their results show that, throughout the cardiac cycle, the basal and apical pressures decrease initially and increase later after the occurrence of E-wave (initial LV filling phase) [13]. At the start of the E-wave, large velocity occurs due to the strong filling jet entering through the mitral valve. An annular vortex is formed and travels smoothly towards the middle of the LV. Moreover, a weak vortex is also generated within the aortic outflow tract. This vortex enlarges but is destroyed by the inflow stream when it moves out off the outflow tract. Towards the end of the filling, three vortices of varying sizes can be

observed. Besides the very first vortex during the initial filling, the occurrence of other vortices is not exactly found in other simulations and experiments due to different flow conditions. Their study illustrates the application of a CFD-FSI software to simulate a 3-D heart.

Saber et al. [14] and Schenkel et al. [15] further made use of patient-specific MRI images to construct the geometry of the LV of a 3-D heart in the numerical simulation. Hence, the geometry of the LV at different instances is prescribed rather than influenced by the FSI. The valves of LV are represented by 2-D planar models. The simulation is based on another commercial CFD solver, Star-CD. In Saber et al. [13], the inflow/outflow rate at the mitral/aortic valves cannot be specified as boundary condition due to the limited measurements. Therefore, a uniform, constant pressure is prescribed at the mitral and aortic valves. Their model is able to capture the 3-D contraction and expansion phases of the LV. However, areas of the mitral and aortic valves are underestimated with overestimated velocities. This could be due to the low resolution of MRI and interpolation uncertainties. On the other hand, Schenkel et al. [15] used a 1-D circulatory system based on Naujokat and Kiencke [16] to provide realistic pressure boundary conditions. Their results show that both the MRI and simulation give reasonable blood flow at the mitral valve. However, the velocity is over predicted for the aorta valve during the systolic phase due to the underestimated diameter of the aortic valve. Regarding to the velocity fields and evolution in the LV, the simulation and MRI data are in good agreement during the initial filling phase. The effect of vortex growth is not as pronounced during diastole in the simulation. Towards the late LV filling, the MRI data does not appear to show a clear image due to the low velocities. Moreover, an additional test based on a different numerical model with a different atrial representation shows a completely different flow configuration, indicating the sensitivity of inflow conditions on the LV. In this case, a simplified model with prescribed LV geometry is able to give good estimation of the flow inside the LV. However, this model is still not matured enough and practical for clinical purpose.

Both Saber et al. [14] and Schenkel et al. [15] indicated the importance of clear MRI images to construct the geometry of LV in the simulation. However, it is common to retrieve MRI images with blurring or ghosting artifacts in reality due to breathing motion and bowel movement [17]. Particularly for time-resolved 3-D data acquisitions, large amounts of data require measurement durations that often exceed normal human breath-holding capabilities. These poor quality images will hinder an accurate analysis of the heart. Markl et al. [18] used an improved navigator-gated time-resolved 3-D phase contact MRI (PC-MRI) velocity mapping based on real-time adaptive k-space reordering in combination with a wider data acceptance window to improve the image quality. The acquisition of images is achieved using an eight-channel phased-array body coil (3T system, TRIO; Siemens, Erlangen, Germany [18]) . This system allows one to reconstruct the 3-D images of the heart over a cardiac cycle as well as time-resolved 3-D hemodynamic velocity fields. In general, the appearances of images are excellent with moderate blurring and minor ghosting artifacts. Currently, available data comprises of both healthy volunteer as well as patients with cardiac problems for comparison in the hospital.

The main objective of this study is to develop a 3-D CFD based, patient-specific cardiovascular modeling system. The tools comprise of a 3-D CFD code to simulate the heart and the 4-D PC-MRI system. This hybrid system could potentially identify possible diseased conditions in LV through the analysis of the vorticity, kinetic energy, hemodynamic, pressure and shear stress. This facilitates physicians to diagnose any probable cardiac problems at an early stage. For example, it has been estimated that about 30% of all heart attacks are fatal [19]. In this way, sudden heart attacks can be avoided and more lives can be saved. Similar to Saber et al. [14] and Schenkel et al. [15], both MRI images and CFD simulation are used in this study. This paper mainly focuses on the accurate model representation of the heart flow within the cardiac cycle and the resulting vortex dynamics in the LV. In order to achieve better accuracy, we take the advantage of the IBM code described by Mcqueen and Peskin [6] rather than a commercial software. The IBM is more suitable for this large movement simulation since it does not suffer from grid quality deterioration, commonly seen in structured grids. Furthermore, the entire heart is simulated in our study. This heart model is constructed based on the anatomy and mechanical properties of the heart muscle fibers, which have been extensively documented by physiologists. It can, therefore, be easily incorporated into any computer model. More details can be found in McQueen and Peskin [6]. Moreover, the moving geometry of the heart (or LV) is changed with time according to the FSI between fluids and muscles. Hence it is more accurate to simulate the changing geometry of the heart.

The heart model has been modified to allow flexibility in specifying the reservoir pressure boundary conditions (RPBC). This is slightly different from Saber et al. [14], which only uses a uniform, constant pressure boundary condition. Using different RPBC enable us to investigate the effect of the boundary condition on the LV. The next section describes the methodology of the cardiovascular modeling system, followed by a detailed description of the 4-D PC-MRI system and its capabilities. The numerical method developed by Mcqueen and Peskin [6] will be explained briefly. Our results involved hemodynamic comparison, vortex, kinetic energy, pressure and shear stress

analysis. Good agreement has been obtained in most cases. The conclusion summarizes the overall performance and specific areas which require further investigation.

PATIENT-SPECIFIC CARDIOVASCULAR MODELING SYSTEM

Methodology

In order to develop an accurate CFD based, patient-specific cardiovascular modeling system, we need to integrate the analyzed data from 4-D PC-MRI system (hardware) into the IBM heart model (software). The system details will be given in later sections. Fig. 1 shows the fundamental methodology. Healthy volunteers, as well as patients with cardiac problems, have been requested to be scanned by the 4-D PC-MRI system. The raw data comprises of the images and the hemodynamic velocity of the heart over an entire cardiac cycle. The 3-D IBM heart model [6] requires the initial and boundary conditions for the pressure. This can be obtained from idealized cases as well as typical estimation of healthy adults documented in the medical literature. This allows us to investigate various scenarios and their effects on the LV of the heart. The semi-realistic simulation provides very useful heart flow information for diagnostic, such as visualization, velocity field, kinetic energy (KE), vorticity and pressure. The comparison between volunteers and patients can help us to identify critical flow conditions resulting from diseased heart and provide deeper insights in the diagnostics.

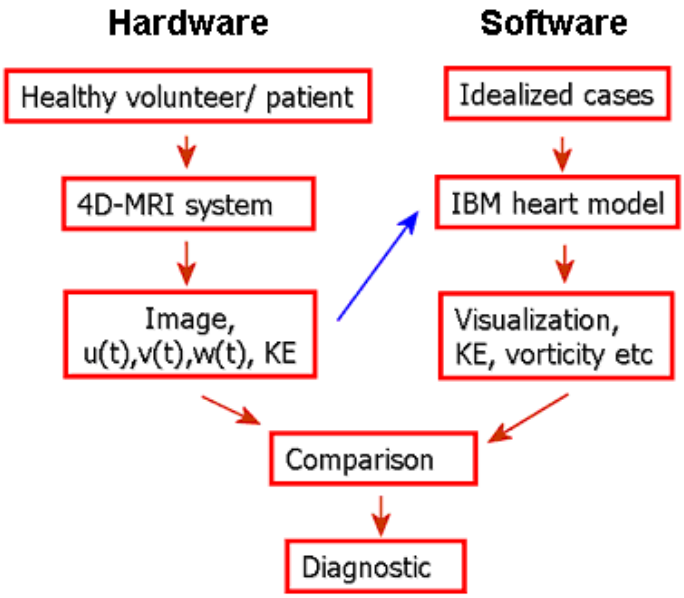

Fig. 1. Fundamental methodology of the CFD based, patient-specific cardiovascular modeling system

In the IBM heart model, the boundary conditions are specified at five major inflow and outflow sources, comprising of 1) superior vena cava (SVC); 2) inferior vena cava (IVC); 3) pulmonary vein (PV); 4) pulmonary artery (PA); and 5) aorta. These five sources primarily dictate how the blood flows in/out of the heart. It is crucial to specify them accurately. The SVC and IVC are two large veins in charge of transporting de-oxygenated blood to the right atrium of the heart respectively [20]. The SVC is formed by the left and right brachiocephalic veins and blood through the SVC enters the right atrium through the upper right front of the heart. Similarly, the blood in the IVC enters through the lower right, back side of the heart. The PV (four in reality, but simplified to only one in the 3-D heart model) carries oxygenated blood from the lungs to the left atrium (LA) of the heart. It delivers de-oxygenated blood from the heart to the lungs. The aorta, the largest blood vessel in the body which originates from the LV of the heart, transports oxygenated blood to all parts of the body. Early research [8, 21-22] has shown that the filling dynamics of LV contains vital health information of the heart. We, therefore, concentrate on the flow dynamics of LV and the PV, which directly affects the blood entering the LV.

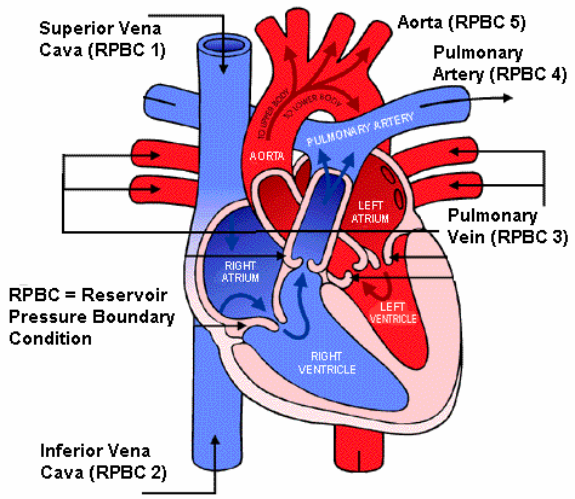

Fig. 2. A diagram of the heart with the five BC sources. (Figure obtained and modified from Abdallah [23])

4-D PC-MRI system

The latest 4-D time-resolved PC-MRI, located at the National Taiwan University Hospital, provides better and more realistic physiological information for the CFD flow simulation. This system acquires images using an eight-channel phased-array body coil, which allows the reconstruction of 3-D images of the heart over a cardiac cycle. However, getting clear and accurate images is not straightforward due to various problems, such as insufficient respiration control, related artifact generation and limited signal-to-noise ratio [18]. Moreover, post-processing will be required to identify, check and extract the relevant heart flow velocity fields over the cardiac cycle. The images are taken at intervals of approximately 45 milliseconds. The spatial resolution of the each image is 256x192x8 (x,y,z), which approximates to an actual size of 307x230x48 mm. Each "z=" plot represents the z coordinate slice of the xy plane.

The test subjects of the 4-D PC-MRI system comprise of both healthy volunteer as well as patients with cardiac problems. This will enable a distinct comparison between the two groups of participants. However, in our initial test and hereafter, we took the data from a healthy volunteer, 35 year-old female. A snapshot image is shown in Fig. 3 taken at T=0.2, where 1T is equivalent to a whole heartbeat. It is one of the heart image slices at the resolution of 256x192. The red arrowed lines represent the velocity vectors of the blood flow. A high concentration of vectors is observed in the circled region and this corresponds to the diastolic phase when large amounts of blood enter the LV.

As mentioned earlier, some researches have emphasized on the distinct differences between vortex formation process in the LV of the heart for the healthy volunteer as well as patients with cardiac problems. With the aid of our CFD heart model, we can now investigate closely the entire process happening within the LV. The main objective is to examine whether disease-related dysfunctions in intervals before complete heart failure can be observed in the dynamics of transmitral blood flow during early LV diastole. Combing the non-invasive 4-D PC-MRI information with the quasi-realistic heart model provides us a unique opportunity to evaluate the cardiovascular hemodynamic in advance.

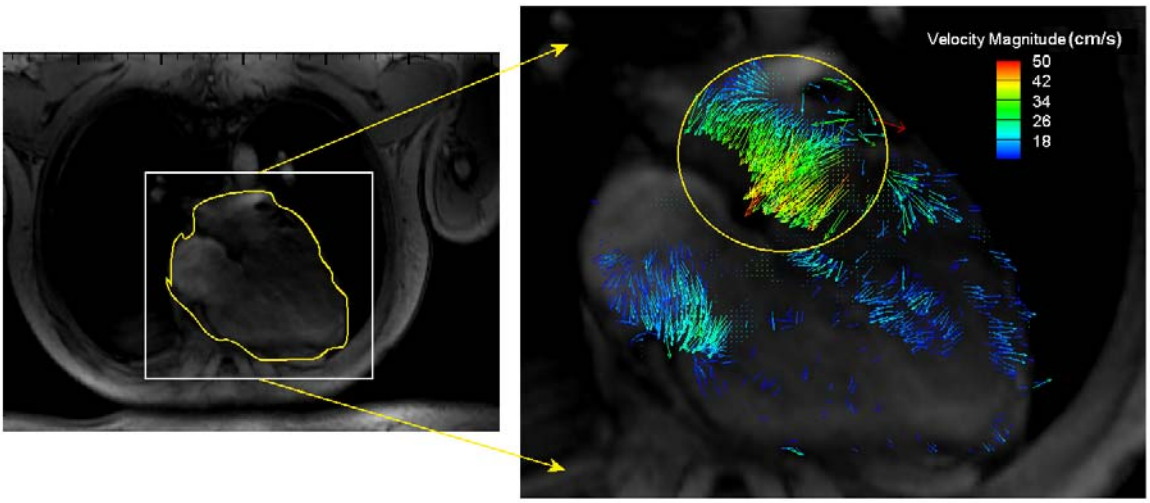

Fig. 3. One of the heart image slices at 256x192 resolution obtained using the 4-D PC-MRI system

3-D CARDIOVASCULAR MODEL AND NUMERICAL METHOD

The 3-D IBM heart simulation is based on the model developed by Mcqueen and Peskin [6]. This model is more adequate for modeling elastic and contractile fibers of the heart than other variations of the IBM [24-25]. The governing equations are based on the 3-D incompressible Navier-Stokes equations with the immersed boundary forcing given by:

$$\rho\left(\frac{\partial \boldsymbol{u}}{\partial t}+\boldsymbol{u}\cdot\nabla\boldsymbol{u}\right)+\nabla p=\mu\Delta\boldsymbol{u}+\boldsymbol{f}\,, \tag{1}$$

$$\nabla\cdot\boldsymbol{u}=\boldsymbol{0}\,, \tag{2}$$

$$\boldsymbol{f}(\boldsymbol{x},t)=\int_0^{L_b}\boldsymbol{F}(s,t)\delta(\boldsymbol{x}-\boldsymbol{X}(s,t))ds\,, \tag{3}$$

$$\frac{\partial \boldsymbol{X}(s,t)}{\partial t}=\boldsymbol{u}(\boldsymbol{X}(s,t),t)=\int_\Omega \boldsymbol{u}(\boldsymbol{x},t)\delta(\boldsymbol{x}-\boldsymbol{X}(s,t))dx\,, \tag{4}$$

$$\boldsymbol{F}(s,t)=\boldsymbol{S}(\boldsymbol{X}(\cdot,t),t)\,. \tag{5}$$

In this case, $\boldsymbol{x} = (x,y,z)$, $\boldsymbol{u}(\boldsymbol{x},t) = (u_1(\boldsymbol{x},t), u_2(\boldsymbol{x},t), u_3(\boldsymbol{x},t))$, is the fluid velocity and $p(\boldsymbol{x},t)$ is the fluid pressure. μ and ρ represent the fluid viscosity and density respectively. The force density (with respect to $d\boldsymbol{x} = dxdydz$) acting on the fluid is $\boldsymbol{f}(\boldsymbol{x},t) = (f_1(\boldsymbol{x},t), f_2(\boldsymbol{x},t), f_3(\boldsymbol{x},t))$. $\boldsymbol{s}$ tracks a material point of the immersed boundary and the boundary force density (with respect to ds) is $\boldsymbol{F}(s,t) = (F_1(s,t), F_2(s,t), F_3(s,t))$.

Eq. (3) and (4) estimate the interaction between the immersed boundary and the fluid. Eq. (5) represents the boundary force resulting from the boundary configuration at time t, where the function $\boldsymbol{S}$ satisfies a generalized Hooke's law if the boundary is elastic.

Two sets of grids, fixed and moving, are adopted in the IBM. The fixed grid represents the Cartesian grid x,y,z which covers the entire fluid domain. On the other hand, the moving grid represents the boundary or fibers of the heart. At each time step, the force acting at each point on the fiber is calculated using Eq. (5). These fibers exert force onto the fluid, represented by the Cartesian fixed grid, and the force on the fluid is calculated using Eq. (3). The resulting velocity at time step $(n+1/2)$ is then obtained by solving Eq. (1) and (2) using the fractional step method, which solves the momentum and the pressure Poisson equations. With this, one can return to interpolate the fiber's velocity from its surrounding fluid's velocity. The fibers then move to their new positions at $t=n+1/2$ based on their velocities. With the known velocities and positions of the fibers at $t=n+1/2$, the solution process is repeated but now they are used to take a full time step from $t=n$ to $n+1$. This results in a time-centered or Crank-Nicolson scheme which has "formal" second-order accuracy [26]. The whole process is shown in Fig. 4.

The construction of the 3-D IBM heart model includes a few steps. The most fundamental component is the boundary points, which are joined together to form fibers. Fibers with the same number of points are clustered together as a group while a bunch is made up of groups. The bunches together form the heart. Hence, the entire heart model is made up of about 4,000 fibers consisting of about 600,000 boundary points. On the other hand, the fixed Cartesian grid uses 128x128x128 grid points. A new single heartbeat, together with the initial transient, requires about 57,000 time steps. Subsequent heartbeats require about 32,000 time steps. The current simulation uses the first heartbeat after the initial transient since there are problems after around 57,800 time steps. This will be discussed in more details in the following paragraphs.

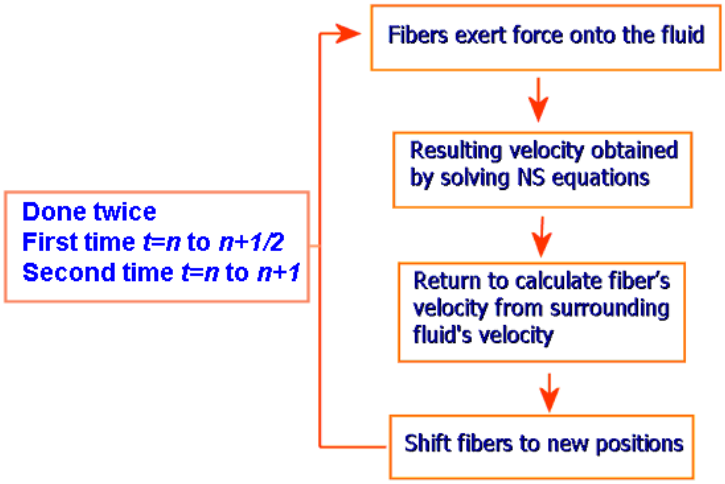

Fig. 4. Flowchart of the IBM numerical method

In Mcqueen and Peskin [6], the reservoir pressure boundary condition (RPBC) are fixed throughout the cardiac cycle, as shown in Fig. 5. This is similar to the boundary condition used by Saber et al. [14]. The influences of different PV pressure BC are investigated here (see Table 1 for the sensitivity runs). Since the current focus is the blood flow in the LV, the variation of PV reservoir pressure will affects its inflow condition. Run 1 refers to the original control condition. Runs 2 and 3 reduce and increase the constant PV reservoir pressure by 25%, respectively. Run 4 uses varying RPBC throughout the whole cycle. The pressure values in Run 4 are obtained during cardiac catheterization [23] and are similar to those documented in the medical literature.

The ±25% in Runs 2 and 3 is chosen to approximate the maximum and minimum PV reservoir pressure of Run 4. This thus allows a more meaningful comparison among them. Varying reservoir pressure based on a realistic data in Run 4 examines the influence of realistic inflow on the IBM heart model. Fig. 5 shows the imposed RPBC within the cardiac cycle for different runs. Fig. 6 compares the PV and aorta RPBC for these simulations in greater details. The sensitivity tests allow a detailed investigation of the impact of the RPBC on the LV in terms of hemodynamic, vorticity, and Kinetic energy (KE).

A few full cardiac cycles are simulated in the current 3-D IBM heart model. The LV is initially empty and requires to be filled up with sufficient blood. Otherwise, the simulation may not run successfully. This filling period runs from t=0 to 0.34s. Therefore, our analysis of the cardiac cycle starts from t=0.34 to t=1.14s (the whole cardiac cycle T lasts approximately 0.8 s). Hereafter, the time is normalized by the whole cardiac cycle (T=1.0) for simplicity.

Table 1. Different sets of data explained

Run	Data Type
1	Unmodified original constant RPBC
2	Similar to Run 1, except that the PV RPBC is 25% smaller
3	Similar to Run 1, except that the PV RPBC is 25% larger
4	Varying RPBC, derived from a healthy volunteer over a cardiac cycle

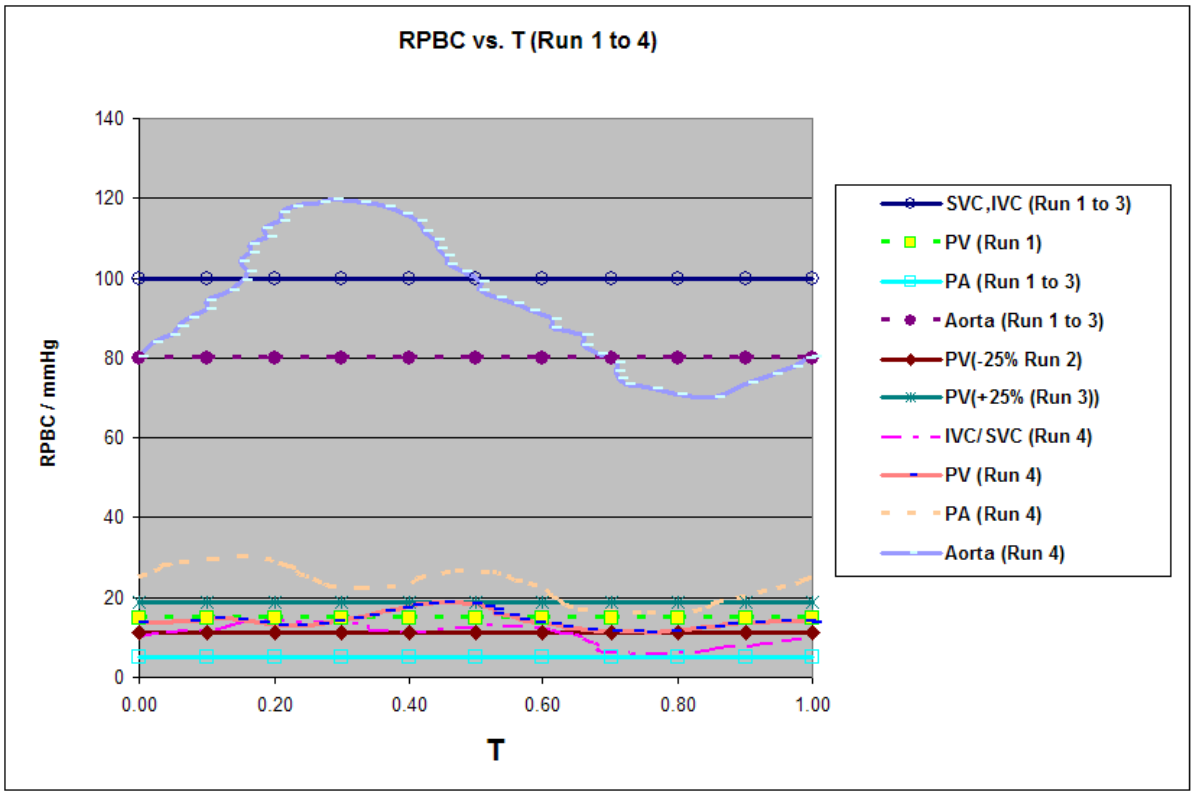

Fig. 5. RPBC at the various sources for Run 1 (original), 2 (-25%) and 3 (+25%) and 4 (realistic)

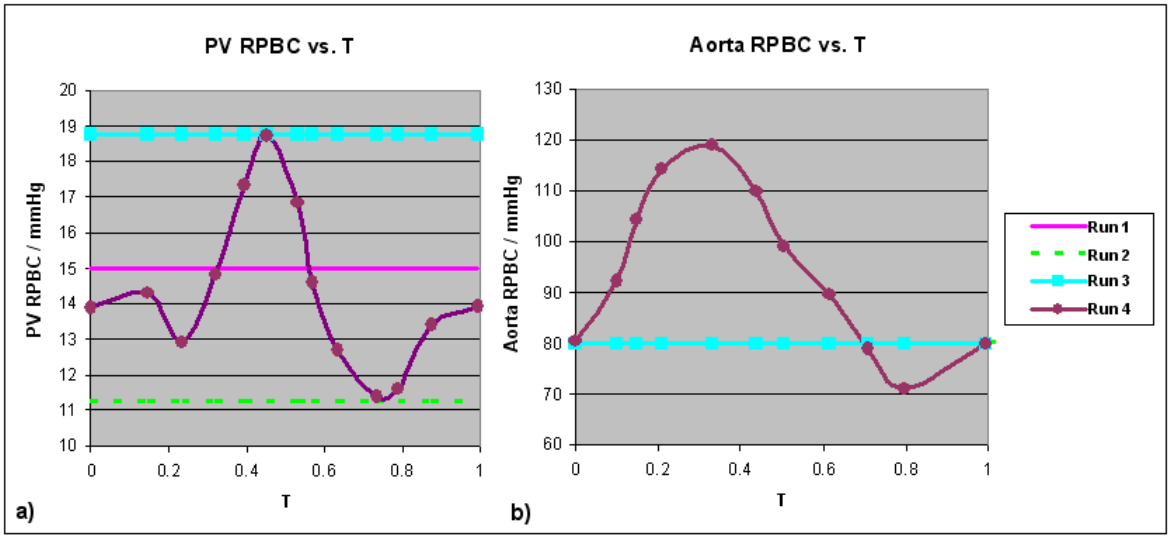

Fig. 6. a) PV and b) aorta RPBC at different times for different runs

RESULTS AND DISCUSSIONS

Hemodynamic comparison

We first concentrate on the comparison of flow rates through the PV and aorta due to different RPBC. In general, the flow of the PV and aorta are qualitatively similar in the whole cardiac cycle except for some phases. Fig. 7 shows the time-varied flow rate of the PV and aorta for different runs.

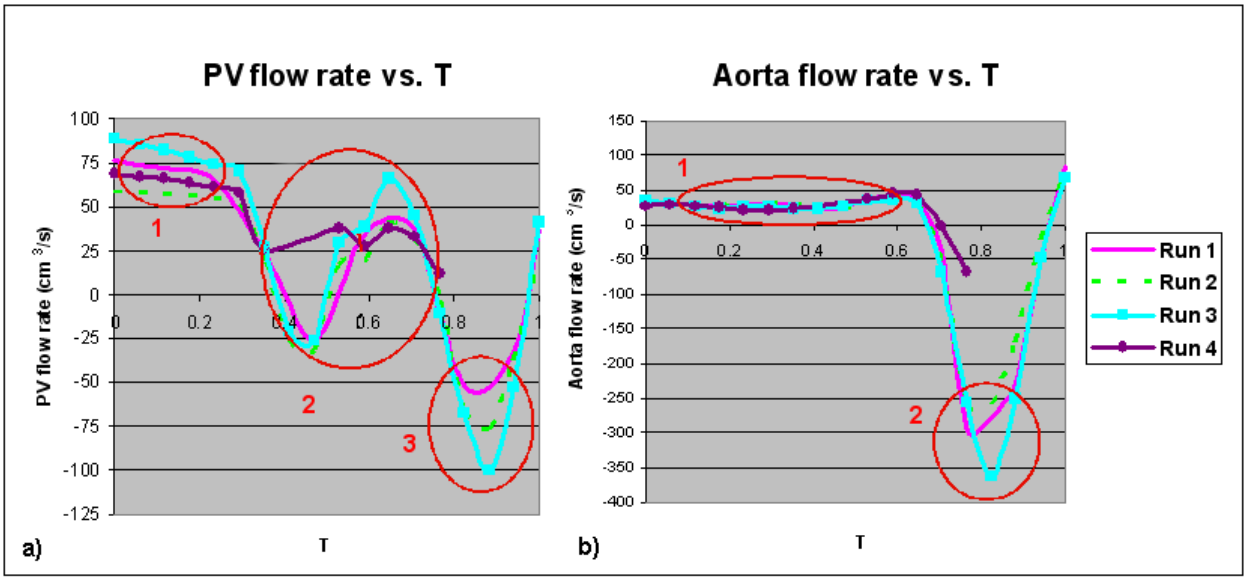

Fig. 7. a) PV and b) aorta flow rate against time for different runs

Between T=0.0 and 0.35 (initial LV filling phase or also known as the E-wave [13], marked as circle 1 in Fig. 7a), the inflow rate at the PV is consistent with the imposed reservoir pressure (Run 2, 4, 1 and 3 from low to high). The highest Run 3 can reach around 80~90 cm^3/s. This indicates that the PV inflow rate directly varies with the RPBC.

During the middle of the LV filling phase (just after T=0.4), the flow rates decrease, reverse (for all cases except Run 4) and then increases again (circle 2, Fig. 7a). This shows that all simulations except Run 4 allow some amount of blood flowing out of the PV, resulting from a higher LA pressure due to the filled-up blood in LA. This is not surprising since the reservoir pressures of Run 1 to 3 are always constant (Fig. 6a). With the higher LA pressure now, the backflow occurs and some blood begins to flow out, resulting in the negative PV flow rate. On the other hand, Run 4 behaves differently since its PV pressure has been on average increasing, from 13 mmHg initially to a maximum of around 19 mmHg around T=0.45 (Fig. 6a). This higher pressure prevents any possible backflow. After T=0.5, the inflow resumes again briefly. This corresponds to the second filling phase, or more commonly known as the A-wave [13], which is due to the atrial contraction. The earlier backflow has lowered the pressure in the LA and hence blood is flowing in again. Similar to the initial filling phase, the inflow rates vary with the specified reservoir pressure for Runs 1 to 3. However, the PV flow rate begins to decrease again after T=0.7. The diastole phase is ending and the systole phase is going to start. There is no more blood flowing in through the PV with rapid decrease of blood.

The inflow decreases to zero and changes to an outflow. A stronger outflow is again observed between T=0.8 to 1.0 (circle 3, Fig. 7a). This is again due to the higher pressure in the LA as a result of the earlier inflow of blood. However, the large magnitudes shown (-50.0 to -100.0 cm^3/s) seem plausible. It seems that the magnitude should be similar to that of the earlier outflow (around T=0.45). This is because the mitral valve is closed at this time, as shown in Fig. 8b (green circle). Hence, there is no additional blood travelling through the mitral valve to the LA and out to the PV. In an actual heart, the mitral valve opens to allow blood to flow into the LV during diastole. Under normal condition, the mitral valve should prevent backflow during systolic phase. This shows that although the mitral valve is nearly close, the 3-D heart model is not able to prevent backflow exactly during the systole phase (e.g. mitral valve dysfunction). Further analysis of the similarity to the corresponding heart problems is required. Note that the solution of Run 4 starts to diverge after T=0.9 and hence is not valid to described its flow rate thereafter. It is interesting to note that in some diseased condition such as LV dilatation, mitral valve dysfunction or pulmonary arterial hypertension, large in/out flow variations are observed clinically, consistent with these idealized constant RPBC.

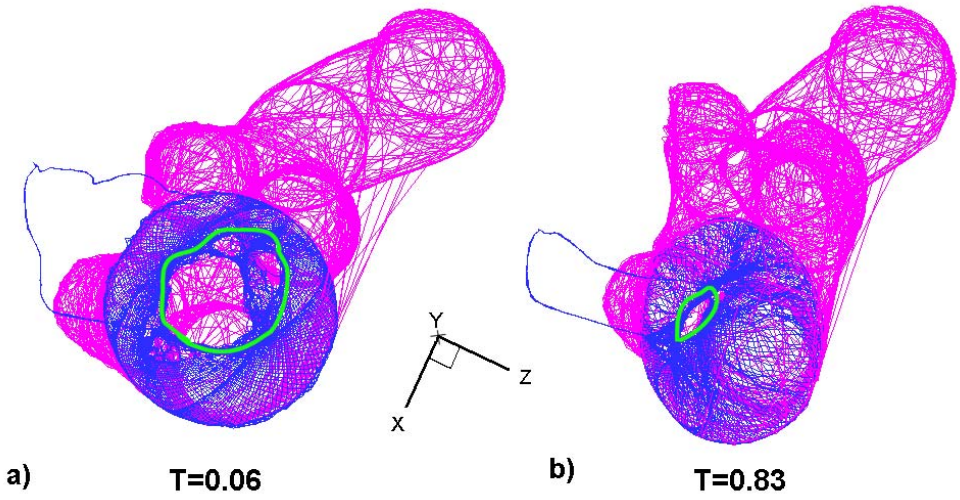

Fig. 8. Mesh of mitral valve (blue) and pulmonary vein (pink) as seen from the bottom in an a) opened and b) closed state

Fig. 6b shows the aorta RPBC condition at different times for different runs. The aorta RPBC for Run 1, 2 and 3 remain constant at 80 mmHg. In this case, the constant value of 80 mmHg is still lower than the average aorta pressure BC of Run 4. However, no significant difference is found in the flow rate of the aorta for different runs from T=0 to 0.65 (Fig. 7b). This is because this period (circle 1, Fig. 7b) corresponds to the initial filling of blood in the LV. The pressure in the LV is still low compared to the aorta's pressure and hence only a small amount of inflow exists.

Due to the divergence of Run 4 after T=0.9, the solution is meaningless beyond T=0.75. For the other runs, after T=0.65, the systole phase begins (circle 2, Fig. 7b). During this period, oxygenated blood starts to flow out through the aorta to other parts of the body. The difference in the PV pressure of Runs 1 to 3 does not significantly affect the outflow. This is simply because the PV and aorta are not close enough so the influence is trivial.

The magnitude of the flow rate for Run 1[*] in Fig. 7 has been non-dimensionalized using the stroke volume[†] and the period of the cardiac cycle T and compared against the clinical data from Fortini et al. [10], as shown as Fig. 9. Baccani et al. [13] and Domenichini et al.[27] also have similar clinical data, except that their data is non-dimensionalized differently. Q represents the flow rate through the mitral during the diastole (0.00T–0.75T), and through the aortic valve during the systole (0.75T–1.00T). The comparison shows that the magnitude of the PV flow rate from Run 1 is generally twice as high as that of Fortini et al. [10]. The variation is also not so pronounced in the PV flow rate for Run 1 between T=0 and 0.3. It is only decreasing slowly and this is mainly due to the prolonged filling phase to ensure the momentum is balanced as mentioned earlier.

Comparison with flow data from Fortini et al.[10] show similar outflow at the aorta during the systolic phase. The high outflow at the aorta occurs at a similar time (T=0.82) with Runs 1 to 3. This indicates that the 3-D IBM heart model can well simulate the different phases of the cardiac cycle. However, the aorta flow rate from Run 1 is much higher than that of Fortini et al.(-5.0 compared to -1.0). In Fortini et al.'s experiment, the inflow during diastole is similar to the outflow during systole. This is also true in Run 1, although its magnitude is much larger. This is most likely to conserve the prolonged filled mass flow rate numerically. Further investigation is still required to verify this speculation.

It is important to note that Fortini et al.'s graph in Fig. 9 is obtained by combining flow rate from the mitral value and aorta during the diastole and systole phase respectively. Hence, flow rates at the mitral valve and aorta during the systole and diastole phase are assumed to be zero respectively. But in the simulation, there is still outflow during the systole for the PV.

[*] Run 2 and 3 are not included in the comparison because their flow rate's graphs are similar to that of Run 1.

[†] The stroke volume refers to the difference in the volume of the LV between the end-diastolic and the end-systole phase and it can be obtained using the method outlined in the later vortex formation time section.

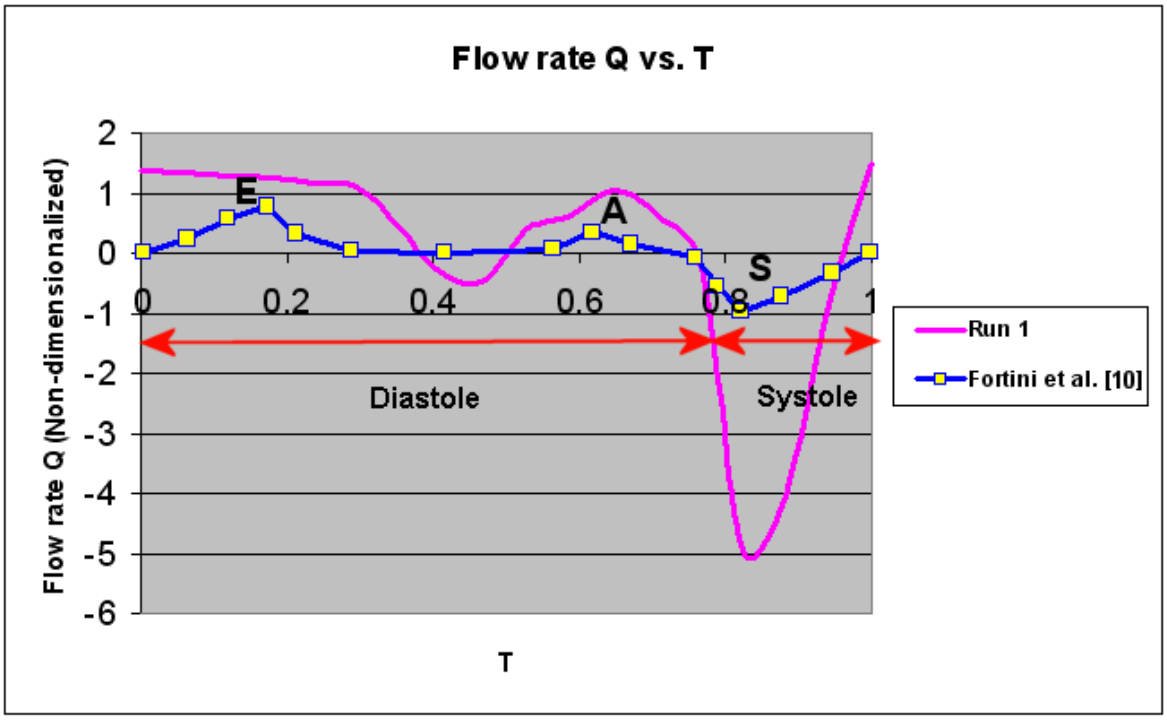

Fig. 9. Comparison between magnitudes of the inlet flow rate *Q* to the LV against time *t* plot, for Run 1 and Fortini et al. [10] . E, A and S refer to the E-wave, A-wave and S-wave respectively.

Analysis of vortex dynamic

2-D Vortex analysis

The evolution of the vorticity in the LV throughout the entire cardiac cycle is discussed here. However, more emphasis is placed on the vorticity dynamics in the LV of the heart during diastole. As mentioned by Domenichini et al. [8], many researches [21-22] have confirmed that the vortices generated in the LV play an important role in the heart functionality. Moreover, Gharib et al. [7] and Pierrakos and Vlachos [9] discussed the formation of vortex during the diastole period and showed that fluid transport is more efficient by vortex ring formation than a steady, straight jet of fluid. Both *in vivo* and *in vitro* data [7] also show that there are distinct differences between the vortex formation time T_v in healthy volunteer and cardiac patients. We first analyzed the modeled vorticity field and then discussed the vortex formation T_v further in depth.

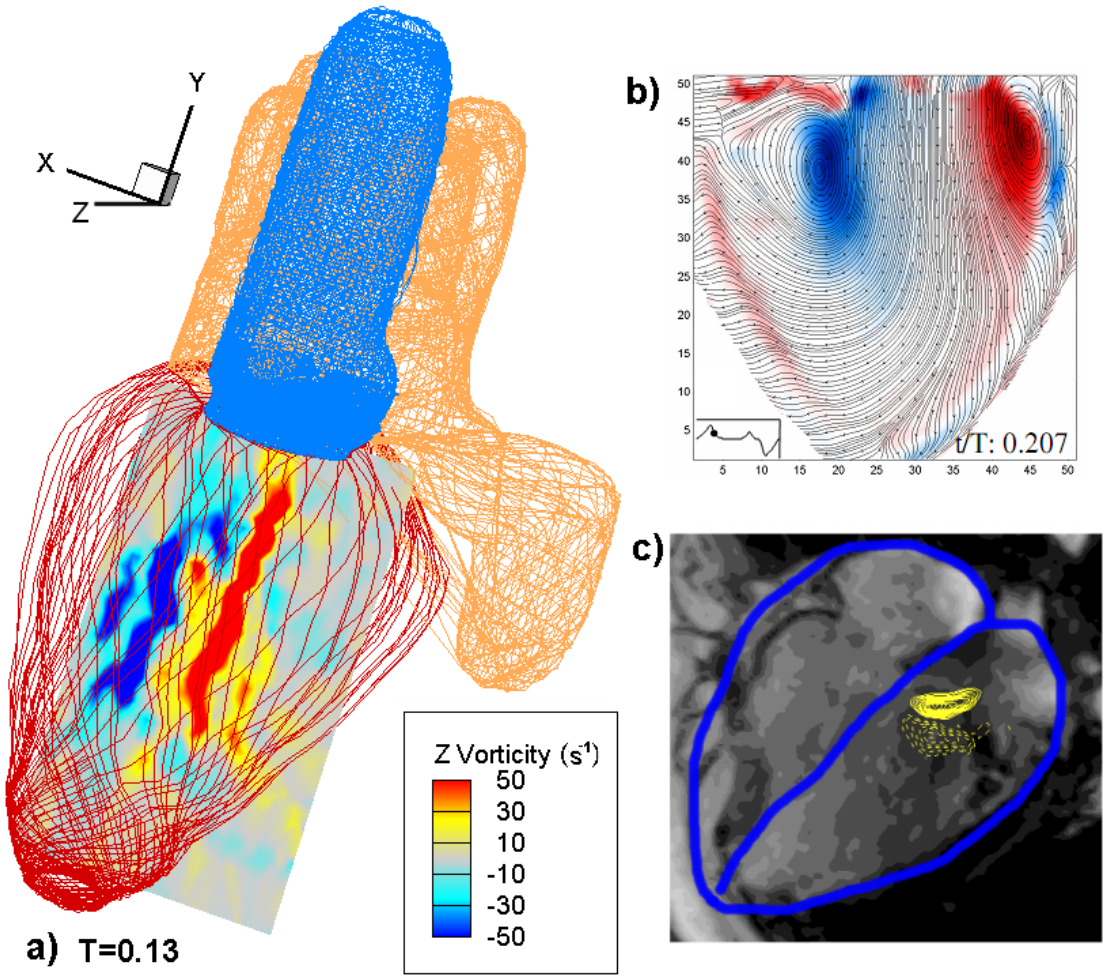

Fig. 10. a) Vorticity contour plots at z=0.56 (along the same plane as the location of the PV) of control Run 1 at T=0.13. Experimental results of vorticity fields from b) Fortini et al. [10] and c) 4-D PC-MRI system

Fig. 10a shows the vorticity of control Run 1 at T=0.13, which is around the early diastolic phase. The 2D vorticity fields (Z vorticity) are obtained by extracting a slice of the heart along the z direction. Denoting the two edges of the heart as z=0 and z=1, the cross-section of the vorticity contour plot represents location z= 0.56 (Fig. 10a). This slice is chosen because it is on the same plane as the PV and can clearly show the vorticity variation. Blue and red represent negative and positive vorticities respectively. Note that the negative vortex is generated on the left while the positive one is on the right. The formation and their respective locations can be explained using Fig. 11. The blood flows into the LV through the mitral valve's opening. As the blood enters the LV, the larger space of the surrounding allows it to "spread" after traveling a short distance. Since the LV is still an enclosed space, the blood interacts with the wall and is constrained to "roll back" giving the vortices shown in Fig. 11. Note that this is a simplified illustration of an axisymmetric valve but the valve in the modeled heart is non-axisymmetric. Numerous experiments have been conducted to show the pair of vortices. For example, Fortini et al. [10] tried to model the LV using conical sack made of silicone rubber and their results showed two vortices of opposite signs, similar to the simulation. The pair of vortices is also shown in the MRI image from a healthy volunteer [7]. Our simulation results tally well with the two experimental results (Fig. 10). However, Fortini et al. [10] also argued that, as the diastolic phase proceeds, the left negatively signed vortex (blue) would grow stronger than the right positively signed one. They suspected that the right (red) vortex interacts viscously with the wall of the LV, slows down and diminishes in size. This does not happen to the left (blue) vortex and hence it is able to grow bigger. Unfortunately, this is not observed in the current simulation. It is possible that the current code is not able to accurately simulate the viscous interaction of the vortex with the wall boundary. Finer mesh may be required.

The pair of vortices slightly changes in shape with time but remains in place until around T=0.49 (roughly the later diastolic phase). At T=0.55, only a weak vortex of negative vorticity remains and diminishes later, as shown in Fig. 12a. At the end of cardiac cycle, blood is flowing out of the aorta and no vortex is observed on the selected plane, which is the same plane as the PV. In order to study the flow around the aorta, a different plane similar to that of the aorta is required. In this case the plane of z=0.79 is extracted. From Fig. 12b, one can now observe that the bulk of the vorticity is near the aorta region, as a result of blood rushing out through the aorta valve. At a later time of T=1.0, due to the contraction of the heart, the plane which coincides with that of the aorta is now at z=0.65. This time corresponds to the end of the systole and hence the flow is now reduced and the vorticity is also relatively weak, as shown in Fig. 12c.

Moreover, the occurrence of multiple vortices, as mentioned by Cheng et al. [12] is not observed. This could be because the 2-D vortex analysis was done at a particular slice of the 3-D ellipsoidal thin-wall ventricular model. As will be shown next, the selection of different cross-sections of the ventricular model will show different vortex evolutions. It is also possible that slightly different computational and experimental conditions can alter the appearance of the subsequent vortices [12].

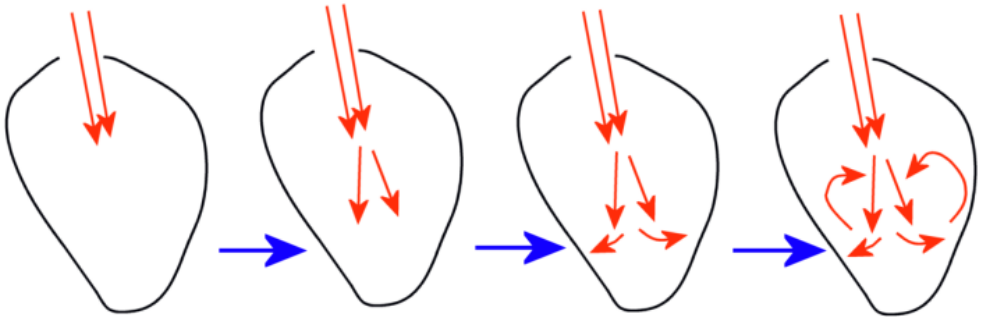

Fig. 11. Simplified evolution of flow over time through a single axisymmetric opening valve

Similar pair of vortices is also observed in the other runs. However, the pair of vortices appears around 0.1T later in Run 2 compared to Run 1. The difference in the appearance time of these vortices is mainly due to different RPBC at the inflow boundary. The specified pressure at the PV pumps the oxygenated blood from the lung into the heart, before travelling to the LV. Hence, its pressure significantly affects the blood flow rate. Since Run 2 uses the lowest constant RPBC of 11.25mmHg, its flow rate is lower than the rest simulations. Hence the appearance of the vortices occurred at a later time as expected.

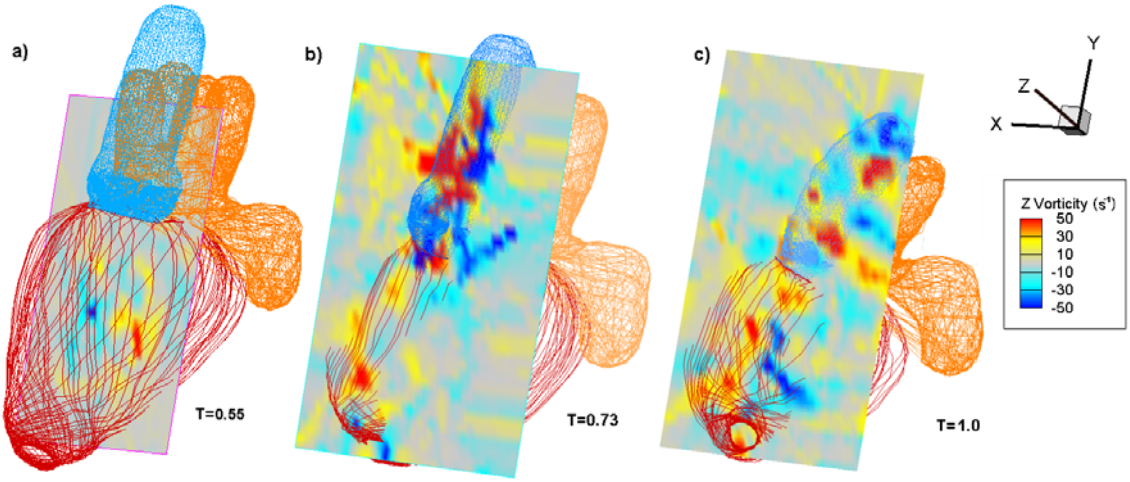

Fig. 12. Vorticity contour plots of Run 1 at a) z=0.56 at T=0.55 b) z=0.79 at T=0.73 c) z=0.65 at T=1.0

3-D Vortex analysis

In this section, we further analyze the 3-D vortex using the iso-surface of vorticity magnitude. Due to the complex evolution of the blood flow in LV, using vorticity magnitude is much easier compared to more complicated methods [28]. Although Jeong and Hussain [28] discussed that vorticity magnitude may not accurately identify vortex cores, we are more interested in the evolution of the vortex rather than identifying the vortex cores. Vorticity magnitude of 40.0 s^{-1} is chosen for better illustration. We focus on the evolution of the vortex between T=0 to 0.6, which is the active diastolic period as shown in Fig. 13.

At T=0.06, we can observed the iso-surface vortex at the center of the LV. The flow has entered the LV and several vortex rings starts to get connected together. The flow then reached a more mature stage and the vortices have stabilized at T=0.37, giving clearer connected vortex rings (blue circle). By the late diastolic phase (roughly T=0.56), the vortex rings are now disconnected, leaving only a small region of weak vorticity. As mentioned by Domenichini et al. [8], the irregularity of the vortices shows the possible existence of weak turbulence fields. Our 3-D vortex visualization gives another view of the vortex evolution. A specified cross-section of the 3-D vortex will give the vorticity contour plot similar to that of Fig. 10a.

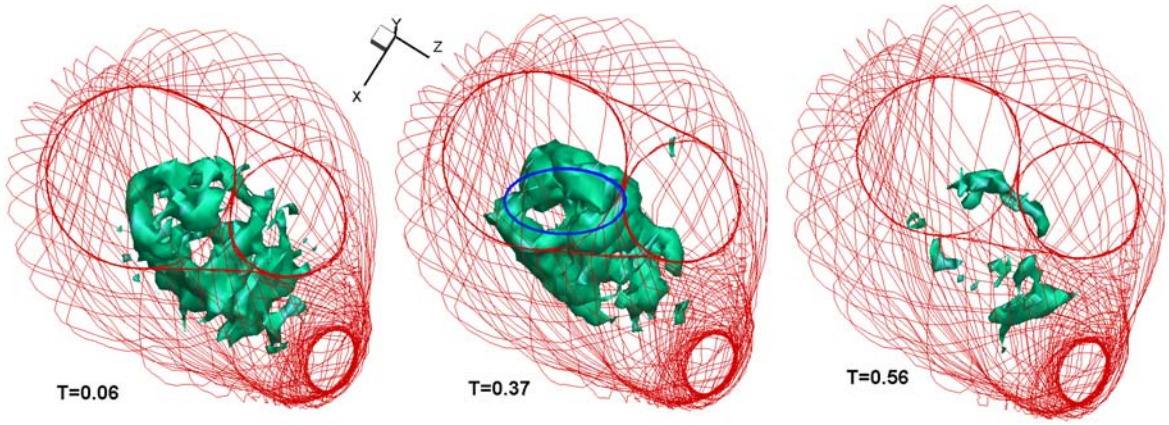

Fig. 13. 3-D vortex evolution in the LV for Run 1

Vortex formation time

As mentioned earlier, the vortex formation time is a good indicator of the cardiac health of the patient. Here, we also calculate the vortex formation time in the simulations. The vortex formation time T_v [7] is given by:

$$T_v = \frac{4(1-\beta)}{\pi} \cdot \alpha^3 \cdot EF \ . \tag{6}$$

The variable α is a LV geometry parameter defined as:

$$\alpha = \frac{EDV^{1/3}}{\overline{D}} . \tag{7}$$

Where *EDV* is the LV end-diastolic volume (LV filling) and $\overline{D}$ is the time-averaged mitral (annulus) valve diameter. The parameter β is the fraction of the stroke volume contributed from the LV "A wave" filling (i.e., atrial contraction) and is equal to 0.2 in a normal heart at rest. Furthermore, *EF* is the ejection fraction, which refers to the ratio of the LV stroke volume to the LV volume at the end of diastole:

$$EF = \frac{EDV - ESV}{EDV} = \frac{SV}{EDV} . \tag{8}$$

where *ESV* is the LV volume at the end of systole (LV ejection), and *SV* is the stroke volume. Getting the volumes of the *EDV* and *ESV* is not straightforward in the simulation due to the fibers arrangement of the modeled heart. Details about the volume calculation can be found in the appendix. Based on the algorithm, the modeled *ESV*,*EDV* and *EF*

values are compared with earlier studies (Table 2). Boron [29] gave typical values of the *ESV* and *EDV* from clinical data while Saber et al. [14] and Schenkel et al. [15] obtained their values by re-constructing the computational geometry using the MRI data.

Table 2. Values of calculated *ESV*,*EDV*,*EF*,α and T_v for Run 1 to 4

Run	Gharib et al.	Boron	Saber et al.	Schenkel et al.	1	2	3	4
ESV/cm^3	-	50	50	64	50	25	51	-
EDV/cm^3	-	120	97	166	106	102	110	-
EF	0.65	0.58	0.48	0.62	0.53	0.75	0.54	-
α	$1.70 < \alpha < 2.00$	-	-	-	1.58	1.56	1.60	-
T_v	$3.30 < T_v < 5.50$	-	-	-	2.11	2.90	2.23	-

The values of the *ESV* and *EDV* for Runs 1-3 are very close to those given by Boron [29] and Saber et al. [14]. This shows that the ability to simulate the volume change of the heart with very good accuracy, despite using idealized boundary condition. The lower PV reservoir pressure in Run 2 has resulted in the over-contraction of the heart and hence the *ESV* is found to be too small. Since the solution diverges for Run 4, the value of *ESV* cannot be obtained correctly and is ignored for the comparison. Compared to the value of 0.65 for the *EF* given by Gharib et al. [7] for the healthy volunteers, the values given by Run 1 and 3 are closer to those given by Boron and Saber et al.

The time-averaged mitral (annulus) valve diameter, $\bar{D}$, can be obtained easily because the mitral annulus is represented as a 2D surface in the simulation. The value of α given in Gharib et al. [7] ranges between 1.7 and 2.0 while those obtained in the simulations are between 1.52 and 1.60. Using these values, the vortex formation time T_v can be calculated between 2.11 and 2.90, acceptable from the expected value between 3.3 and 5.5 (Gharib et al. [7]). Note that the vortex formation time formula is very sensitive to small differences in α. The power cube in Eq. (6) may magnify the small differences in values. Other sources of errors are due to the estimation of the volume *ESV*, *EDV* and $\bar{D}$. This is unavoidable due to the irregular boundary of the heart.

Kinetic energy

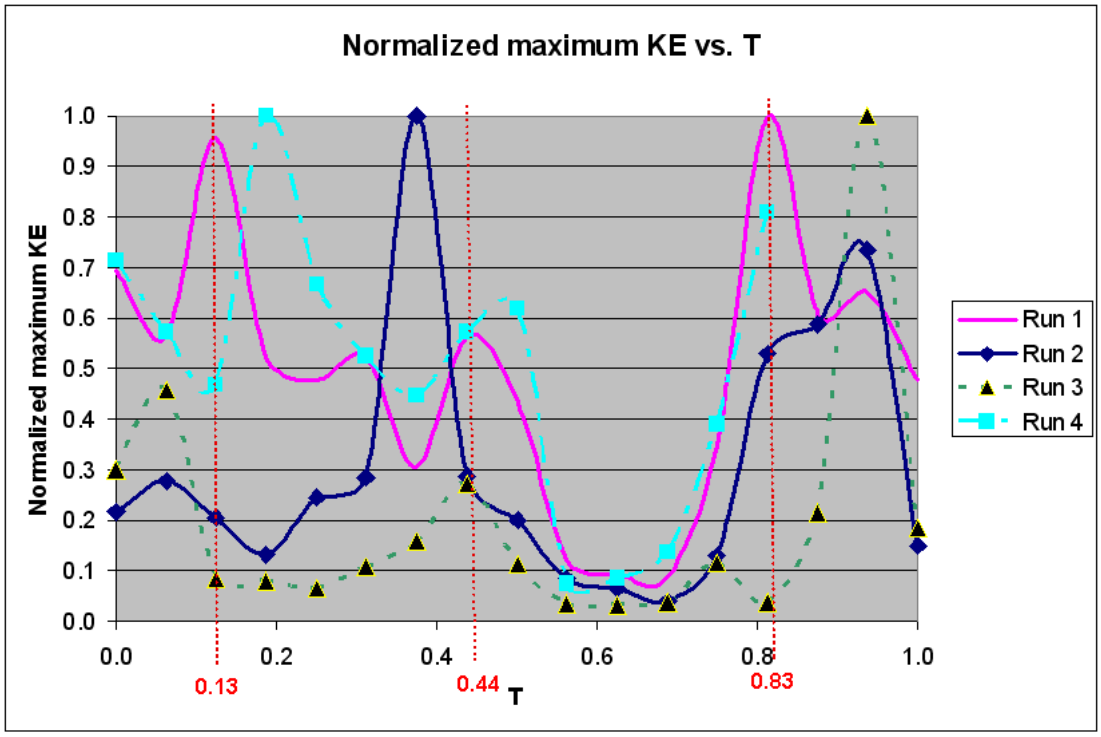

Fig. 14. Normalized maximum KE vs. time T in the LV for different runs at slice z=0.56

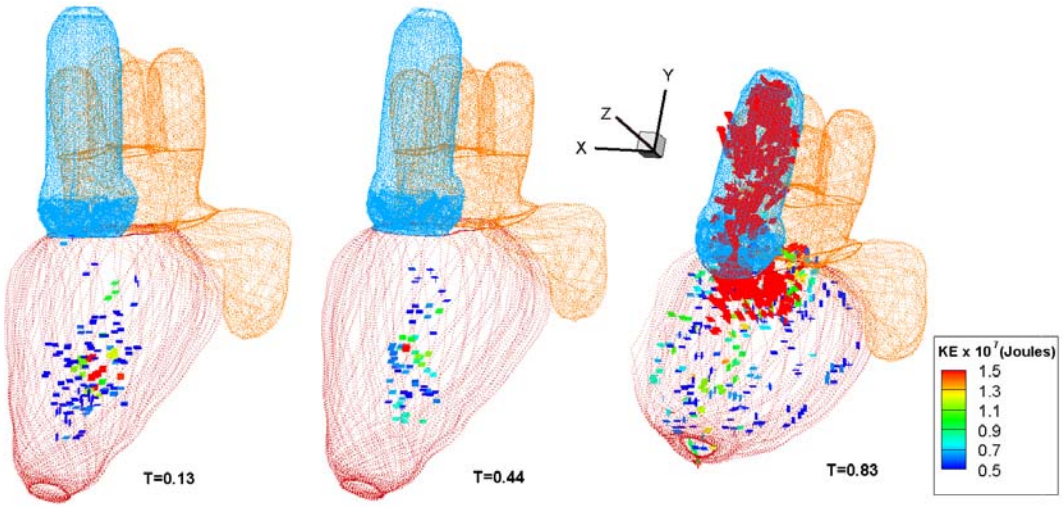

Fig. 15. KE of the markers in the LV for Run 1 at different times showing the three peaks. KE values below 3.0×10^{-7} joules are not shown. The color of the markers indicates the level of its KE.

The variation of the kinetic energy (KE) of the blood flow in the LV indicates the work done by the pumping heart. Fig. 14 shows the time-evolved maximum KE within the whole cardiac cycle in the LV for the four runs at z=0.56. This plane is selected because it can capture the variation of the KE more clearly. Three peaks of the maximum KE can be observed at T=0.13, 0.44 and 0.83 for the control Run 1. The actual locations where the maximum KE occurs can be observed in Fig. 15. It corresponds to a region of vorticity and energy. The first two timing (T=0.13 and 0.44) show that high volume of blood flows into the LV through the PV. This generates vortices which help to minimize the energy dissipation during flow transport [30]. The first peak corresponds to high inflow of the blood into the LV during the initial diastole (also known as E-wave) while the second lower peak (A-wave) corresponds to the period during atrial contraction. Since a higher flow rate is akin to higher kinetic energy, one can also compare with the flow rate against time plot in Fig. 9. These two peaks are also observed in the data by Fortini et al [10]. In this case, the peaks (E and A) occurred at around T=0.16 and 0.62 (interval of 0.46T). Hence, its time interval is also slightly longer. This may result from a number of possibilities. First of all, the data from the 4-D PC-MRI system may not be universal due to the uncertainty of patients, timing and others. From the simulation side, the imposed boundary conditions will influence the variation in KE as well. The third peak in Fig. 14 corresponds to the large outflow of oxygenated blood through the aorta valve during the systolic period. The same timing is also captured in Fig. 9, which is around T=0.83.

Run 2 also has three peaks at T=0.04, 0.38 and 0.95. The second peak is much higher than the first, which seem erroneous when compared to other runs and the clinical data in Fig. 9. More investigations are required in this case why a lower RPBC gives this result. Similarly, Run 3 has three peaks of similar relative peak values as compared to Run 1. However, the timings of the peaks are slightly different. This shows that the boundary condition may significantly affect the timing of the A-wave and E-wave. Run 4, which uses variable RPBC obtained from realistic data of a healthy volunteer, show the first two peaks, similar to that of Run 1, except at a slight delay of around 0.05T. Moreover, the magnitudes of the first two peaks for Run 1 and 4 are similar. However, due to the divergence of the solution, it is not able to obtain solution after 0.8T.

Different slices of the normalized total KE of the heart using the 4-D PC-MRI system are also shown in Fig. 16. Due to the limitation of the system, it is not possible to obtain maximum KE only in the LV. Hence it is not possible to do a direct comparison between Fig. 14 and Fig. 16. Nevertheless, interesting information can be obtained by using slices of different planes. The z=5 (z=5 out of 8 slices = 0.625) plane in this case is similar to the plane shown in Fig. 14 (z=0.56). There are also three peaks. These correspond to the initial diastolic, atrial contraction and systolic phases.

As mentioned earlier, several potential factors matter. More investigation is required due to several uncertainties in either data or simulation (e.g. difference categories of volunteers such as male and female, age and the boundary conditions imposed). Nevertheless, Run 1,3 and 4 are able to show the peaks correctly.

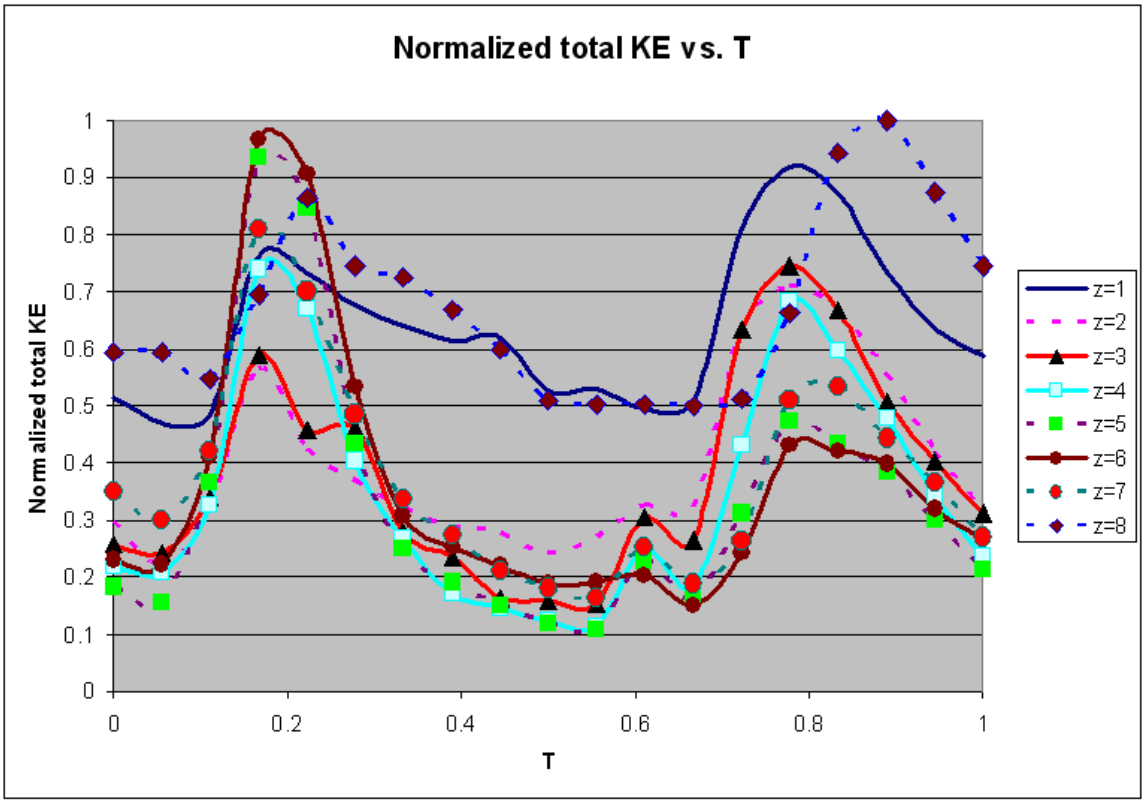

Fig. 16. Normalized total KE at different slices, obtained from the 4-D PC-MRI system

Pressure and shear stress analysis

The pressure and shear stress on the wall surface of LV are important for the heart functions. Due to the complicated fibers arrangement of the heart and the immersed boundary technique, the pressure on the LV surface cannot be obtained directly. The pressure magnitude on the wall surface is approximated in a similar fashion to the estimation for the vortex formation time, except that we further approximated the small pieces of polygon surface to ellipses at each plane. This is done by searching for the maximum and minimum distances of the polygon points from the center at each plane. These distances form the major and minor axis of an ellipse respectively. This approximation of ellipse with points at equal intervals can ensure an equally distributed surface pressure calculation while the original approximation of the polygon has sides of different lengths. Then the pressure distribution can be obtained by interpolating the Cartesian grid pressure results.

Due to the complicated procedures, analysis is only done on Run 1. Our results show that, on average, the wall pressure of LV remains relatively constant during the earlier cardiac cycle (T=0 to 0.6). This is because the heart is still relaxed during the diastole phase as blood flows into the LV. However, the graph on Fig. 18 show that the surface maximum pressure increases between T=0.1 and 0.3. Closer examination of the pressure shows that this increase in pressure only occurs at a small region near the aorta, as shown by the black circle 1 in Fig. 17. This may indicate that the aorta region is under high pressure. However, this is also possibly due to an error resulting from the pressure approximation. Further investigation is required. Nevertheless, after T=0.3, the surface pressure throughout

remains low at around 10mmHg from T=0.4 to 0.6 because of the reduced flow rate (Fig. 9). During this time, the heart expansion also slows down. However, the pressure increases significantly from T=0.7 to 0.85 (see Fig. 17) while the heart is transitioned to the systole phase. The muscles and fibers need to contract rapidly in order to pump oxygenated blood from the heart to other parts of the body through the aorta. Fig. 19 shows the contracted heart in the simulation at two different time slices. Note that the muscles in the heart are not only contracted but also twisted during the systole. The simulated heart at T=0.83 is deformed further than that at T=0.2. Hence, the pressure at that moment is extremely high. The average pressure at T=0.2 is around 10 mmHg throughout the entire surface. However, at T=0.83, the pressure has increased to as high as 150 mmHg, as seen in the red region in Fig. 17c. Moreover, the pressure distribution in this case is not even. The front view shows intense high red region (around 150 mmHg) while the sides have lower pressure ranging from 20 to 60 mmHg. This is due to some surface region twisting and contracting more than the other regions. At around T=0.85, the pressure rapidly decreases, increases to 80 mmHg before dropping again. The subsequent increase in pressure occurs near the aorta region (black circle 2) is probably because of reversed outflow (inflow) through the aorta, as shown in Run 1, Fig. 9. After T=0.95, the pressure over the entire surface decreases as the heart relaxes. This shows that the high surface pressure distribution towards the end of the cardiac cycle is not affected by different RPBC. The surface pressure strength is mainly determined by the cardiac phase resulting from the flow contraction and twisting.

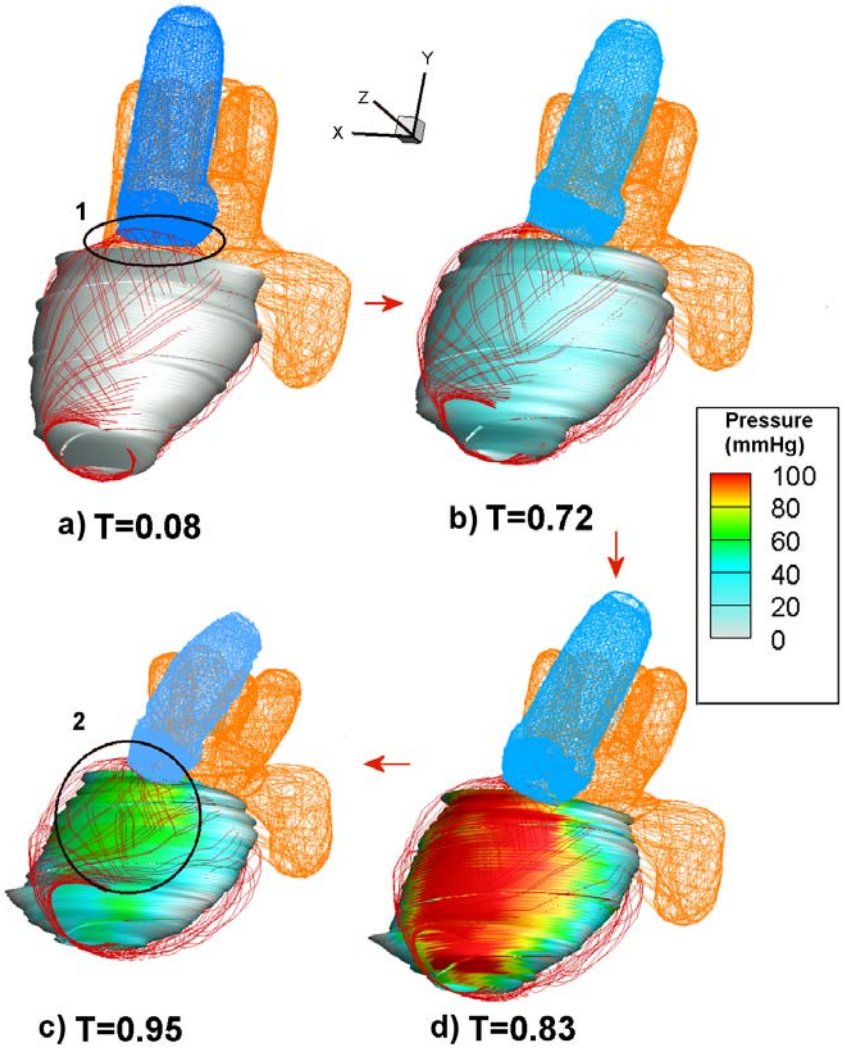

Fig. 17. Change in surface pressure over a cardiac cycle for Run 1

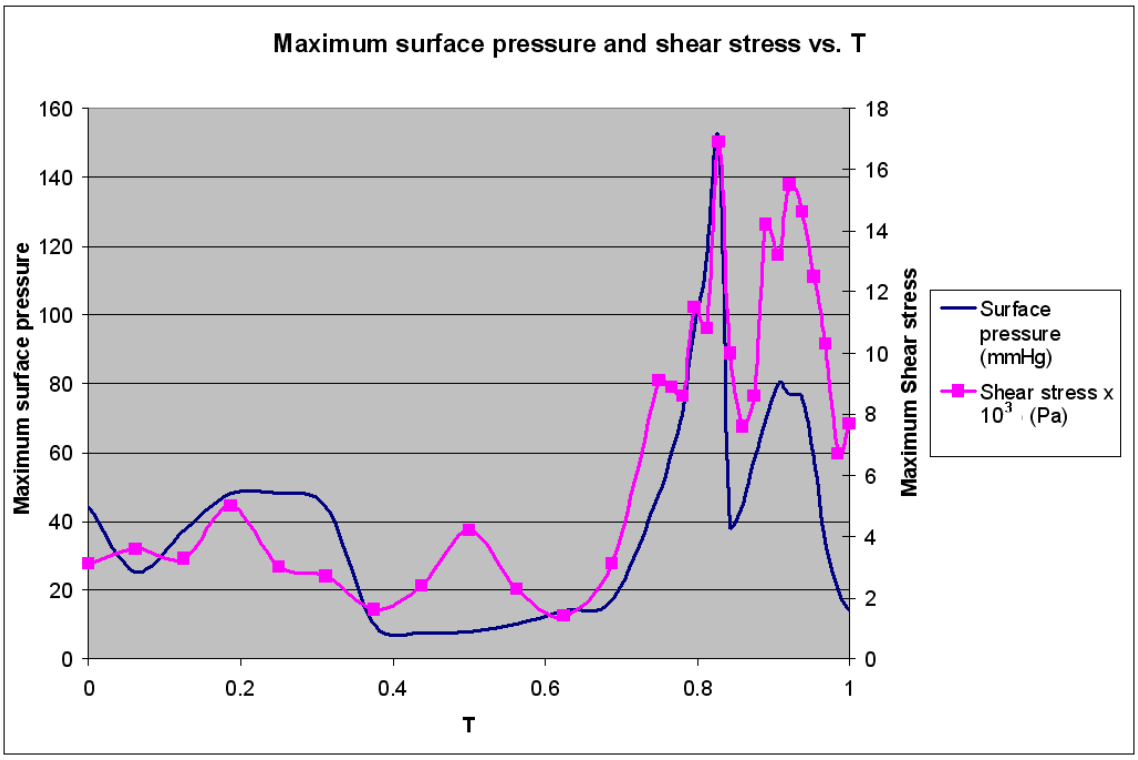

Fig. 18. Graphs of maximum pressure and shear stress vs. T for Run 1

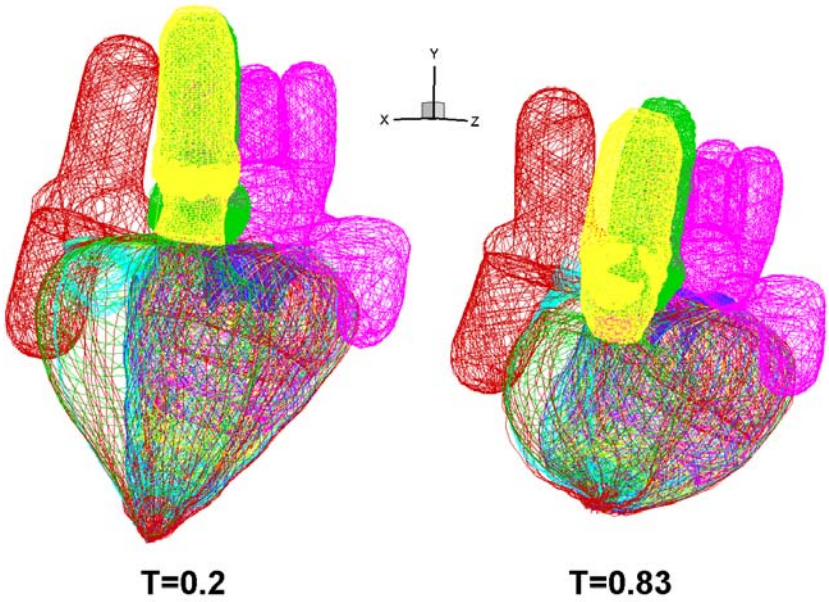

Fig. 19. Simulated heart with the fiber muscles[‡] of Run 1 at T=0.2 and 0.83

The shear stress distribution on the wall of LV is also analyzed similarly. Fig. 20a shows the LV making up of fibers. The original wall shear stress formula can be found in [31] and it is modified[§] to give:

[‡] The different colors represent the different sections of the heart such as the aorta, pulmonary artery and vena cava.
[§] In our analysis, we are interested in the magnitude of the shear stress and hence the terms are squared and their sum then square-root.

$$\sigma_{ss} = \sqrt{\left(\frac{\mu(v_m - v_1)}{|\boldsymbol{d}|}\right)^2 + \left(\frac{\mu(u_m - u_1)}{|\boldsymbol{d}|}\right)^2} \tag{9}$$

where μ[**] is the dynamic viscosity of the blood, $\boldsymbol{v_1}$, $\boldsymbol{v_a}$, $\boldsymbol{v_b}$ are the velocity vectors of the consecutive fiber points of the ellipse. $\boldsymbol{v_m}$ is the average velocity of $\boldsymbol{v_a}$ and $\boldsymbol{v_b}$. $\boldsymbol{d}$ is the vector from $\boldsymbol{v_1}$ to $\boldsymbol{v_m}$. Note that u_1, v_1, u_m *and* v_m (scalars) are all perpendicular to $\boldsymbol{d}$. A graphical representation of the variables is shown in Fig. 20b. $\boldsymbol{v_1}$ is situated around the LV's wall and hence it can be approximated as the wall velocity. The points on the ellipse represent the wall boundary of the LV. To compute the shear stress, two points are selected. They are $\boldsymbol{v_1}$ and $\boldsymbol{v_m}$. $\boldsymbol{v_m}$ is the mid point of $\boldsymbol{v_a}$ and $\boldsymbol{v_b}$. u_1 and u_m are obtained by taking the dot product of $\boldsymbol{v_1}$ and $\boldsymbol{v_m}$ respectively with $\boldsymbol{c}$, which is the vector connecting plane i and i+1. This will allow the evaluation of the velocities parallel to $\boldsymbol{c}$. Similarly, v_1 and v_m are obtained by taking the dot product of $\boldsymbol{v_1}$ and $\boldsymbol{v_m}$ respectively with the position vector of $\boldsymbol{v_a} - \boldsymbol{v_b}$. Eq. (9) can then be applied to obtain the shear stress at a point.

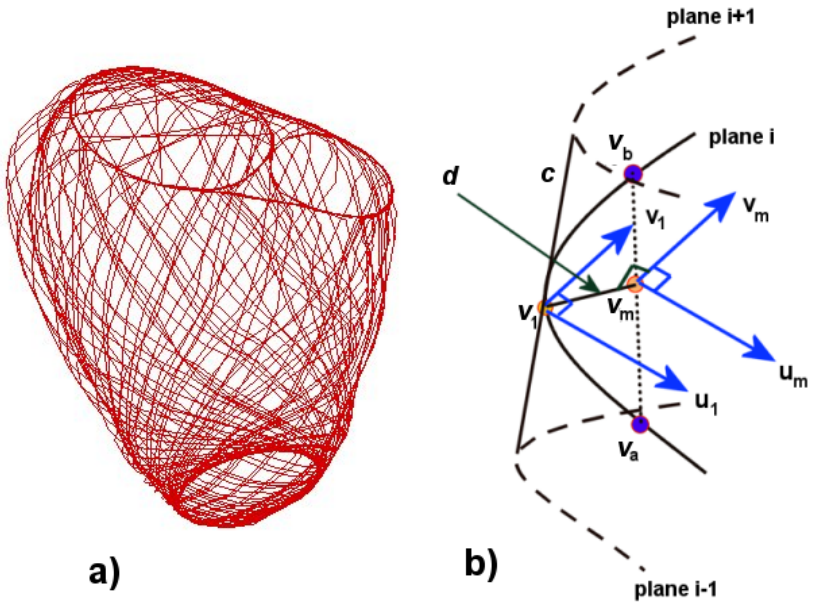

Fig. 20. a) Left ventricle making up of fibers and b) graphical representation of the variables used to calculate the shear stress σ_{ss}

Our results show that, similar to the surface pressure case, the average wall shear stress is very low between T=0.0 to 0.7 in the early diastole phase (Fig. 18), although some small areas have their maximum shear stress reaching 5×10^{-3} Pa . However, no high shear stress is observed at the region near the aorta. Large variation only occurs from T=0.7 to 1.0 (the transition from the heart contraction to relaxation), very similar to that of the maximum pressure. At this moment, the average magnitude of velocities is also much higher. This type of large variation is realistically possible and it has also been shown in the simulation of the human coronary plaque, where the increase in the maximum principle stress can be 800% or more at specific locations [33].

Fig. 21 shows the change in wall shear stress at four different time slices. It is clear to see the existence of twisting and stretching, resulting in the high shear stress. This is expected since the heart muscles are supposed to be tensed at this moment. Moreover, between T=0.82 and 0.95, different parts of the surface of the LV are under high shear stress. At T=0.82, the high shear stress region is very close to the aorta, mainly due to the high outflow of blood out of the aorta. As shown in Fig. 18, the subsequent peak after the first peak at T=0.82 also appears, similar to

[**] A constant value of 2.5×10^{-6} Pa s is used for μ, assuming temperature of blood is 30.0 degrees Celsius [32] Somer, F. M. J. J. D., 2003, "Strategies for Optimisation of Paediatric Cardiopulmonary Bypass," Ph.D. thesis, Rijksuniversiteit Groningen, Netherlands..

that found in the pressure graph. The high shear stress region of this subsequent peak at T=0.95 appears near the aorta as well as near the apex of the heart. This can be due to the aftermath of the high outflow through the aorta. However, the location of high maximum shear stress is different from that of pressure at the same time, indicating that high maximum shear stress is not equivalent to that of pressure. Higher wall shear stress is often associated with coherent swirling of blood, which helps to avoid dissipating excessive energy by limiting flow separation and instability [30].

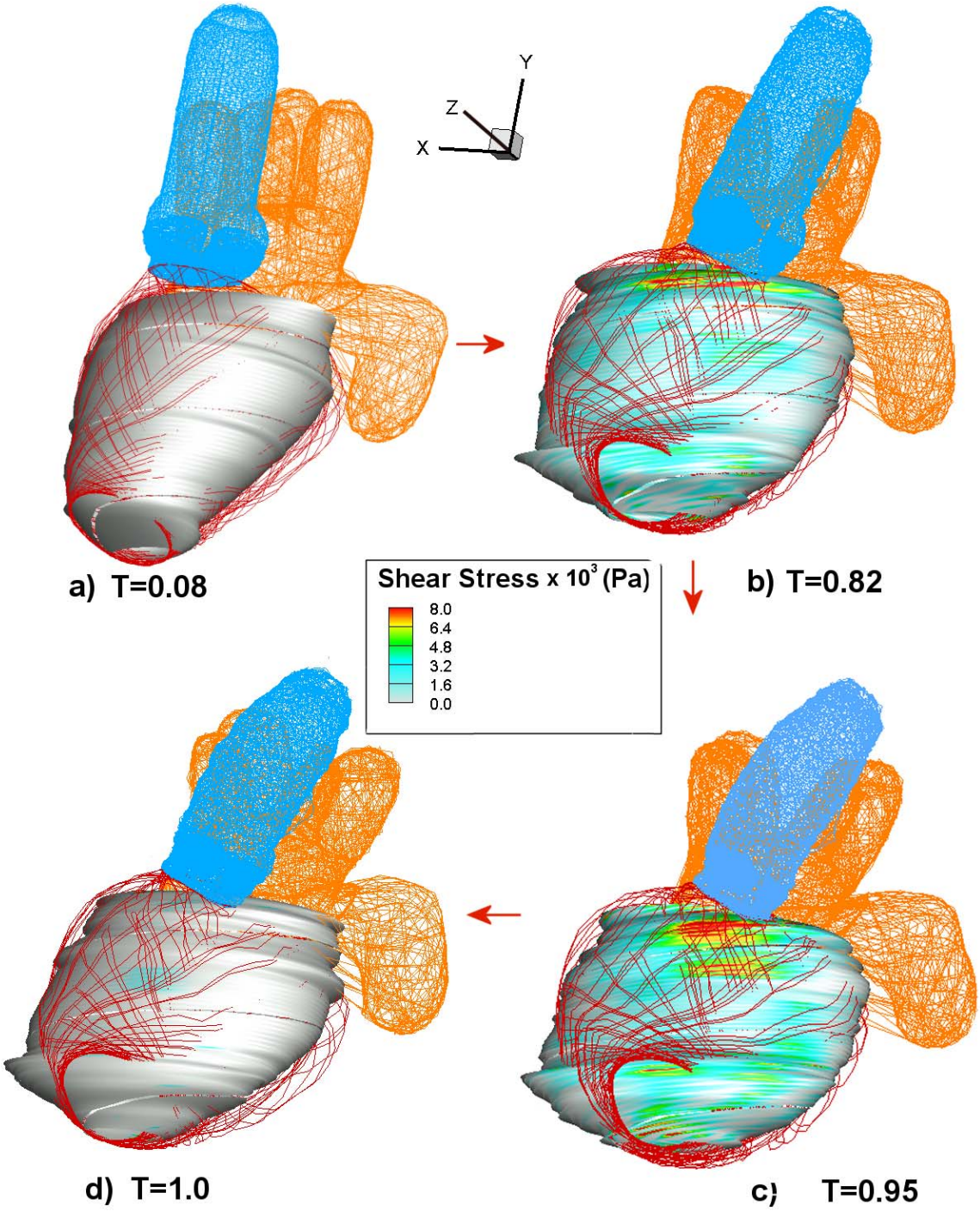

Fig. 21. Change in shear stress over a cardiac cycle

CONCLUSIONS

Simulations have been carried out using the modified code by Mcqueen and Peskin [6] based on different types of RPBC. The results are compared in terms of hemodynamic, vorticity visualization, formation time, kinetic energy, pressure and shear stress analysis. In most cases, considerable differences are found between these runs.

The variation of the flow rate in the PV and aorta compares well with the experimental data. The peaks during the E, A and S waves are captured by the simulation. However, the magnitudes do not tally well. The RPBC has a much greater effect on the flow rate at the PV, as compared to the aorta. Higher RPBC at the PV gives higher flow rate during the initial LV filling phase. Outflow is detected at the PV during the filling phase for all except Run 4, which uses the realistic RPBC. This happens despite the mitral valve's closure. During systole, outflow occurs at the aorta due to oxygenated blood rushing out to different parts of the body.

Modeled vorticity fields show similar results as the experiments conducted by Fortini et al. [10] and Gharib et al. [7]. Both simulation and experimental results show two oppositely signed vortices in the LV. However, the size difference of the left and right vortices is not captured by the simulation. The vortex formation time in Runs 1-3 (2.11 – 2.90), which is used to measure the cardiac health of the patient, compares reasonably within the expected range of values (3.30-5.50) for healthy volunteers.

In terms of kinetic energy, Run 1 and 3 show similar number of peaks (three) as those found in the volunteer's result. The relative heights of the first two peaks (first higher than the second) are also correctly reflected when compared with the clinical data. Although Run 2's result has three peaks too, the first one is lower than the second one. While Run 3 gives the same relative height variation as Run 1, its third peak is exceptionally high. Run 4 shows the same first two peaks as Run 1. However, due to divergence of solution, it is not able to show a possible third peak. Both similarities and differences between the KE and clinical data's flow rate are also seen. More investigations are required to determine if it is due to variance in the volunteer's data.

The analysis of surface pressure on the wall of LV shows that average pressure is very small during the diastole phase. However, a small region near the aorta experiences a small variation in the surface pressure during this time. More investigation is required to determine its cause. Large variations occur towards the end of the cardiac cycle (systole phase), when the heart is highly contracted. This is mainly due to the strong twisting and stretching motion. Similarly, the shear stress analysis also shows similar variation as that of the surface pressure during the cardiac cycle, although the locations of the maximum wall shear stress and surface pressure do not coincide.

In general, the results show that certain runs produce more realistic data than others. Run 4, despite being approximated by a varying and presumably more realistic RPBC does not give better results. Its solution also diverges much earlier than the other runs. Further investigations are required to explain the reason behind the discrepancies. Future work also includes input of patient specific data into the cardiovascular modeling system and the use of hemodynamic data rather than pressure as the boundary conditions to take advantage of the 4-D PC-MRI system. The pressure and shear analysis can be performed on the Run 2-4 and compared against Run 1. Lastly, finer mesh will be used to do the simulation to obtain better accuracy.

APPENDIX

Calculation of volumes of the *EDV* and *ESV*

The calculation of the volumes of the *EDV* and *ESV* is not straightforward due to the fibers arrangement of the heart in the CFD code. More details about the fibers arrangement can be found in McQueen and Peskin [6]. An algorithm has been formulated to approximate the volumes required. The steps to calculate the volume are as follows:

1. The heart is divided into many planes (40-60) along the y direction.
2. Find the intersection points of the fibers with each y plane.
3. On each plane, find the center of the points by taking the average of the locations of all the point.
4. By doing a clockwise rotation scan at every pre-determined angles, select the points such that it is closer to the center and the scanned line. The value of the pre-determined angles chosen depends on the number of sides of the polygon required (Fig. 22a).
5. After the polygon for each *y* plane is found, the approximate volume of the LV can be calculated by using the successive volume formed by the polygons (Fig. 22b).

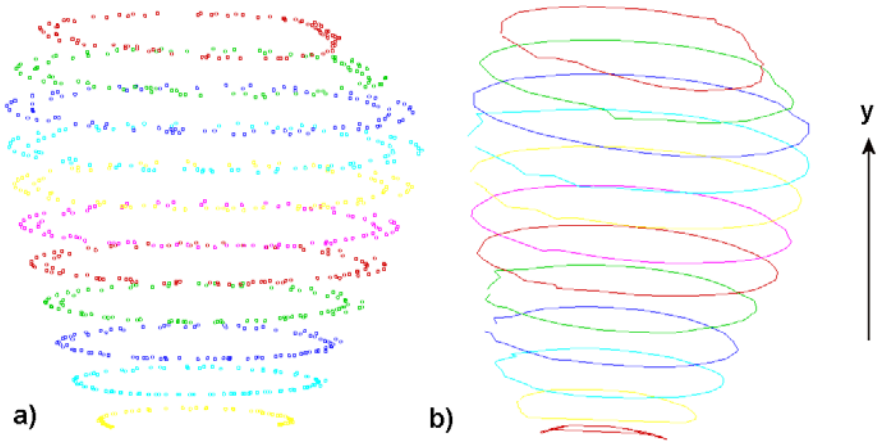

Fig. 22. a) Intersection points of the fibers with each *y* plane b) the polygon of each plane

REFERENCES

[1] Bolzon, G., Zovatto, L., and Pedrizzetti, G., 2003, "Birth of Three-Dimensionality in a Pulsed Jet through a Circular Orifice," Journal of Fluid Mechanics, 493 pp. 209-218.
[2] Bellhouse, B. J., 1972, "Fluid Mechanics of a Model Mitral Valve and Left Ventricle," Cardiovascular Research, 6 (2), pp. 199-210.
[3] Wieting, D. W., and Stripling, T. E., 1984, "Dynamics and Fluid Dynamics of the Mitral Valve," Recent Progress in Mitral Valve Disease, pp. 13-46.
[4] Reul, H., Talukder, N., and Muller, E. W., 1981, "Fluid-Mechanics of the Natural Mitral-Valve," Journal of Biomechanics, 14 (5), pp. 361-&.
[5] Mcqueen, D. M., Peskin, C. S., and Yellin, E. L., 1982, "Fluid-Dynamics of the Mitral-Valve - Physiological-Aspects of a Mathematical-Model," American Journal of Physiology, 242 (6), pp. 1095-1110.
[6] Mcqueen, D. M., and Peskin, C. S., 2000, "A Three-Dimensional Computer Model of the Human Heart for Studying Cardiac Fluid Dynamics," Computer Graphics-Us, 34 (1), pp. 56-60.
[7] Gharib, M., Rambod, E., Kheradvar, A., Sahn, D. J., and Dabiri, J. O., 2006, "Optimal Vortex Formation as an Index of Cardiac Health," Proceedings of the National Academy of Sciences of the United States of America, 103 (16), pp. 6305-6308.
[8] Domenichini, F., Pedrizzetti, G., and Baccani, B., 2005, "Three-Dimensional Filling Flow into a Model Left Ventricle," Journal of Fluid Mechanics, 539 pp. 179-198.
[9] Pierrakos, O., and Vlachos, P. P., 2006, "The Effect of Vortex Formation on Left Ventricular Filling and Mitral Valve Efficiency," Journal of Biomechanical Engineering, 128 (4), pp. 527-539.
[10] Fortini, S., Querzoli, G., Cenedese, A., and Marchetti, M., 2008, "The Effect of Mitral Valve on Left Ventricular Flow," eds., Lisbon, Portugal, pp.
[11] Pedrizzetti, G., and Domenichini, F., 2006, "Flow-Driven Opening of a Valvular Leaflet," Journal of Fluid Mechanics, 569 pp. 321-330.
[12] Cheng, Y. G., Oertel, H., and Schenkel, T., 2005, "Fluid-Structure Coupled Cfd Simulation of the Left Ventricular Flow During Filling Phase," Annals of Biomedical Engineering, 33 (5), pp. 567-576.
[13] Baccani, B., Domenichini, F., Pedrizzetti, G., and Tonti, G., 2002, "Fluid Dynamics of the Left Ventricular Filling in Dilated Cardiomyopathy," Journal of Biomechanics, 35 (5), pp. 665-671.
[14] Saber, N. R., Gosman, A. D., Wood, N. B., Kilner, P. J., Charrier, C. L., and Firmin, D. N., 2001, "Computational Flow Modeling of the Left Ventricle Based on in Vivo Mri Data: Initial Experience," Annals of Biomedical Engineering, 29 (4), pp. 275-283.
[15] Schenkel, T., Malve, M., Reik, M., Markl, M., Jung, B., and Oertel, H., 2009, "Mri-Based Cfd Analysis of Flow in a Human Left Ventricle: Methodology and Application to a Healthy Heart," Annals of Biomedical Engineering, 37 (3), pp. 503-515.
[16] Naujokat, E., and Kiencke, U., 2000, "Neuronal and Hormonal Cardiac Control Processes in a Model of the Human Circulatory System," Int. J. Bioelectromagn., 2 pp. 1-7.
[17] Kitajima, H. D., Sundareswaran, K. S., Teisseyre, T. Z., Astary, G. W., Parks, W. J., Skrinjar, O., Oshinski, J. N., and Yoganathan, A. P., 2008, "Comparison of Particle Image Velocimetry and Phase Contrast Mri in a Patient-Specific Extracardiac Total Cavopulmonary Connection," Journal of Biomechanical Engineering, 130 (4), pp. 041004-14.

[18] Markl, M., Harloff, A., Bley, T. A., Zaitsev, M., Jung, B., Weigang, E., Langer, M., Hennig, J., and Frydrychowicz, A., 2007, "Time-Resolved 3d Mr Velocity Mapping at 3t: Improved Navigator-Gated Assessment of Vascular Anatomy and Blood Flow," Journal of Magnetic Resonance Imaging, 25 (4), pp. 824-831.
[19] Who, 2002, *Integrated Management of Cardiovascular Risk*, World Health Organization,
[20] Wikipedia, 2009, Superior Vena Cava 11th October,
http://en.wikipedia.org/w/index.php?title=Superior_vena_cava&oldid=315757293
[21] Mandinov, L., Eberli, F. R., Seiler, C., and Hess, O. M., 2000, "Diastolic Heart Failure," Cardiovascular Research, 45 (4), pp. 813-825.
[22] Vasan, R. S., and Levy, D., 2000, "Defining Diastolic Heart Failure - a Call for Standardized Diagnostic Criteria," Circulation, 101 (17), pp. 2118-2121.
[23] Abdallah, H., 2009, Pressures and the Heart: How Pressures Change in the Heart, 5th June,
http://www.childrensheartinstitute.org/educate/bloodprs/prchange.htm
[24] Tseng, Y. H., and Ferziger, J. H., 2003, "A Ghost-Cell Immersed Boundary Method for Flow in Complex Geometry," Journal of Computational Physics, 192 (2), pp. 593-623.
[25] Udaykumar, H. S., Mittal, R., Rampunggoon, P., and Khanna, A., 2001, "A Sharp Interface Cartesian Grid Method for Simulating Flows with Complex Moving Boundaries," Journal of Computational Physics, 174 (1), pp. 345-380.
[26] Lai, M. C., and Peskin, C. S., 2000, "An Immersed Boundary Method with Formal Second-Order Accuracy and Reduced Numerical Viscosity," Journal of Computational Physics, 160 (2), pp. 705-719.
[27] Domenichini, F., Querzoli, G., Cenedese, A., and Pedrizzetti, G., 2007, "Combined Experimental and Numerical Analysis of the Flow Structure into the Left Ventricle," Journal of Biomechanics, 40 (9), pp. 1988-1994.
[28] Jeong, J., and Hussain, F., 1995, "On the Identification of a Vortex," Journal of Fluid Mechanics, 285 pp. 69-94.
[29] Boron, W. F., 2003, *Medical Physiology : A Cellular and Molecular Approach*, W.B. Saunders, Philadelphia, PA.
[30] Kilner, P. J., Yang, G.-Z., Wilkes, A. J., Mohiaddin, R. H., Firmin, D. N., and Yacoub, M. H., 2000, "Asymmetric Redirection of Flow through the Heart," Nature, 404 (6779), pp. 759-761.
[31] White, F. M., 2008, *Fluid Mechanics*, McGraw-Hill Higher Education, Boston :.
[32] Somer, F. M. J. J. D., 2003, "Strategies for Optimisation of Paediatric Cardiopulmonary Bypass," Ph.D. thesis, Rijksuniversiteit Groningen, Netherlands.
[33] Tang, D., Yang, C., Kobayashi, S., Zheng, J., Woodard, P. K., Teng, Z., Billiar, K., Bach, R., Ku, D. N., Kitajima, H. D., Sundareswaran, K. S., Teisseyre, T. Z., Astary, G. W., Parks, W. J., Skrinjar, O., Oshinski, J. N., and Yoganathan, A. P., 2009, "3d Mri-Based Anisotropic Fsi Models with Cyclic Bending for Human Coronary Atherosclerotic Plaque Mechanical Analysis Comparison of Particle Image Velocimetry and Phase Contrast Mri in a Patient-Specific Extracardiac Total Cavopulmonary Connection," Journal of Biomechanical Engineering, 131 (6), pp. 061010-11.